

Multi-omic profiling highlights factors associated with resistance to immuno-chemotherapy in non-small-cell lung cancer

Received: 27 April 2023

Accepted: 18 October 2024

Published online: 10 December 2024

 Check for updates

Yilv Yan^{1,11}, Dongqing Sun^{2,3,11}, Junjie Hu^{1,11}, Yue Chen^{4,11}, Liangdong Sun¹, Huansha Yu¹, Yicheng Xiong¹, Zhida Huang¹, Haoran Xia¹, Xinsheng Zhu¹, Dongliang Bian¹, Fenghuan Sun¹, Likun Hou⁵, Chunyan Wu⁵, Orion R. Fan⁶, Haiyang Hu¹, An Zeng¹, Lele Zhang¹, Yi Eve Sun¹, Chenfei Wang¹, Peng Zhang¹

Although immune checkpoint blockade (ICB) therapies have shifted the treatment paradigm for non-small-cell lung cancer (NSCLC), many patients remain resistant. Here we characterize the tumor cell states and spatial cellular compositions of the NSCLC tumor microenvironment (TME) by analyzing single-cell transcriptomes of 232,080 cells and spatially resolved transcriptomes of tumors from 19 patients before and after ICB–chemotherapy. We find that tumor cells and secreted phosphoprotein 1-positive macrophages interact with collagen type XI alpha 1 chain-positive cancer-associated fibroblasts to stimulate the deposition and entanglement of collagen fibers at tumor boundaries, obstructing T cell infiltration and leading to poor prognosis. We also reveal distinct states of tertiary lymphoid structures (TLSs) in the TME. Activated TLSs are associated with improved prognosis, whereas a hypoxic microenvironment appears to suppress TLS development and is associated with poor prognosis. Our study provides novel insights into different cellular and molecular components corresponding to NSCLC ICB–chemotherapeutic responsiveness, which will benefit future individualized immuno-chemotherapy.

Immune checkpoint blockade (ICB) treatments have revolutionized non-small-cell lung cancer (NSCLC) care, even curing some patients with advanced-stage disease^{1–6}. Neoadjuvant immuno-chemotherapy has shown greater effectiveness than ICB alone, with a response rate averaging 32% (18–63%)⁷. Many patients with NSCLC remain resistant to neoadjuvant immuno-chemotherapy and the molecular mechanisms behind this resistance are still unclear.

The tumor microenvironment (TME) includes diverse immune and stromal cells that contribute to tumor growth and immune escape⁸.

Given the cell type diversity in the TME, pioneering studies have used single-cell RNA sequencing (scRNA-seq) to identify features linked to immunotherapy resistance. A recent study on NSCLC following neoadjuvant programmed cell death protein 1 (PD-1) blockade found that tissue-resident T cells are abundant in lung cancer TMEs but have reduced function⁹. Another study identified that a subset of dysfunctional CD8⁺ T cells experience clonal revival after PD-1 blockade in NSCLC¹⁰. These studies collectively indicate that although neoadjuvant ICB therapy could partially reprogram the TME and increase CD8⁺ T cell

A full list of affiliations appears at the end of the paper.  e-mail: azeng@sibcb.ac.cn; zhanglele@tongji.edu.cn; yi.eve.sun@gmail.com; 08chenfeiwei@tongji.edu.cn; zhangpeng1121@tongji.edu.cn

infiltration, the environment remains somewhat suppressive, limiting long-term effectiveness. This underscores the need to explore other TME-associated cell types, such as stromal cells.

Although scRNA-seq has revealed crucial insights into TME heterogeneity across various cancers, its limitation lies in the loss of spatial and morphological information, making it challenging to study cell colocalization and construct spatial architectures of TME. For example, tertiary lymphoid structures (TLSs) are crucial for T cell priming, B cell activation and T and B cell differentiation^{11,12}. TLSs are positively correlated with prognosis in most solid tumors and can predict responses to ICB therapies^{13,14}. However, most scRNA-seq studies have not yet elucidated the geometric structures of TLSs or the mechanisms behind their formation, maturation and function in the TME, due to the lack of spatial organization information for B and T cells.

In this study, we integrate scRNA-seq and spatial transcriptomics to profile the cellular composition and spatial organization of tumor cells and the microenvironment before and after neoadjuvant ICB-chemotherapy in both responders and non-responders. We identify cancer cell states and important spatial compositions of stromal and immune cell types associated with poor responses to ICB-chemotherapy. Through computational analyses, we investigate the maturation processes and potential functions of TLSs in NSCLC. Our study provides novel insights into the complex NSCLC ecosystem and identifies potential biomarkers for future combinatorial therapies.

Results

Study design and overview of the study cohort

To reveal alterations in NSCLC before and after ICB-chemotherapy, we employed scRNA-seq to profile 26 tumor samples from 19 patients with NSCLC before and after neoadjuvant therapy of anti-PD-1 and chemotherapy (Fig. 1a,b). Based on pathologic assessment, which is reliable in assessing ICB-chemotherapy treatment efficacy and predicting survival^{15,16}, six patients were classified as responders (including five with a pathologically complete response (pCR) and one with a major pathologic response (MPR)) and the remaining 13 patients were non-responders (having exhibited a non-major pathologic response (NMPR)) (Fig. 1b). Three responders and four non-responders had matched pre- and post-treatment tumor specimens (Fig. 1b). After quality control, we derived transcriptomes of 232,080 individual cells, with a median of 2,645 reads and 1,205 genes captured per cell. Unsupervised clustering analyses were performed to decipher the cellular compositions, and canonical cell-type-specific markers were used for cell type annotation (Fig. 1c,d and Extended Data Figs. 1a,f and 2a–f).

We obtained 64,947 epithelial cells that formed two distinct major clusters (Fig. 1c), presumably representing normal and malignant cells with different transcriptomic features. To better characterize the heterogeneity of epithelial cells, we re-clustered these cells. We separated normal and malignant cells based on their copy

number variations (CNVs) using InferCNV¹⁷ (Fig. 1e and Extended Data Fig. 1b,c). Unsupervised analyses identified 21 epithelial subclusters: eight normal with distinct markers and 13 malignant (Extended Data Fig. 1d,e). In the epithelial cell compartment, malignant cells were essentially eliminated in responders following ICB-chemotherapy (Fig. 1e). We also observed alterations within the immune and stromal compartments (Extended Data Fig. 1g). In the immune cell compartment, post-treatment non-responders exhibited an increased fraction of monocytes/macrophages and dendritic cells compared with pre-treatment levels (Fig. 1f). Furthermore, in the CD31⁺ stromal cell compartment, the proportion of collagen type XI alpha 1 chain-positive (COL11A1⁺) cancer-associated fibroblasts (CAFs) was significantly higher in non-responders compared with responders, both at baseline and post-treatment (Fig. 1g). These results suggested the potential roles of such cells in affecting the responsiveness to ICB-chemotherapy. Although scRNA-seq provided valuable insights into the cellular compositions of the NSCLC TME, it lacked information on the spatial distribution of cells within the tumor. Therefore, we performed spatial transcriptomic analyses using the GeoMx digital spatial profiler (DSP) platform and 10x Genomics Visium platform, respectively, on 14 treatment-naïve specimens and 17 post-treatment specimens (Fig. 1b,h,i). In-depth analysis of scRNA-seq and spatial transcriptomics revealed several intriguing findings, as detailed in the following sections.

Defining cancer cell states related to treatment outcomes

Transcriptional heterogeneity in tumors is increasingly considered the foundation supporting tumor initiation, progression, metastasis and treatment resistance. Recent research has identified gene modules as the key characteristics that define cell states^{18–21}. Utilizing scRNA-seq data, we initially examined the cell states of cancer cells. Through Harmony, we classified these cells into 14 subsets and annotated them via gene set enrichment analysis, with highly expressed markers (Fig. 2a,b).

The cell states clustered into two groups: one comprising interferon (IFN), alveolar, estrogen, extracellular matrix and coagulation cell states and the other comprising squamous, nuclear factor erythroid 2-related factor 2 (NRF2) target and cell-cycle-related cell states (Fig. 2c). Cancer cell state scores in these two groups were strongly anticorrelated (Fig. 2c). Some cancer cell state scores (for example, hypoxia, squamous, cell cycle, E2F target, NRF2 target and Myc target scores) were associated with poor survival across patients from The Cancer Genome Atlas Lung Adenocarcinoma (TCGA-LUAD) cohort (Fig. 2d). Conversely, cancer cell states including coagulation, alveolar, extracellular matrix, estrogen and IFN were linked to prolonged survival.

To investigate the role of cancer cell states in treatment, we compared cell state scores of cancer cells during immunotherapy using scRNA-seq data. We found that the NRF2 target score was significantly

Fig. 1 | Cellular and molecular characterization of NSCLC tissues before and after ICB-chemotherapy using combined scRNA-seq and spatial transcriptomic analysis. **a**, Workflow of the research design. **b**, Sample information for each patient who participated in this study. The dots for each associated assay indicate data availability. **c**, UMAP plot of all 232,080 cells from all sequenced samples, color coded to indicate the major cell lineages. **d**, UMAP plots of T, B, monocyte/macrophage (mono/macro), CD31⁺ stromal, dendritic (DC) and endothelial cells, color coded to indicate subpopulations. **e**, UMAP plot of epithelium cells, color coded green and brown to indicate normal and malignant cells, respectively. **f**, Boxplot demonstrating the fractions of immune cell subtypes in matched samples from three responders and four non-responders at baseline (before treatment) and post-treatment. The center lines indicate median values and the lower and upper hinges represent 25th and 75th percentiles, respectively. The whiskers denote 1.5× the interquartile range. A one-sided Wilcoxon test was used to determine statistical significance. **g**, Boxplot showing the fractions of fibroblast subtypes in the CD31⁺ stromal

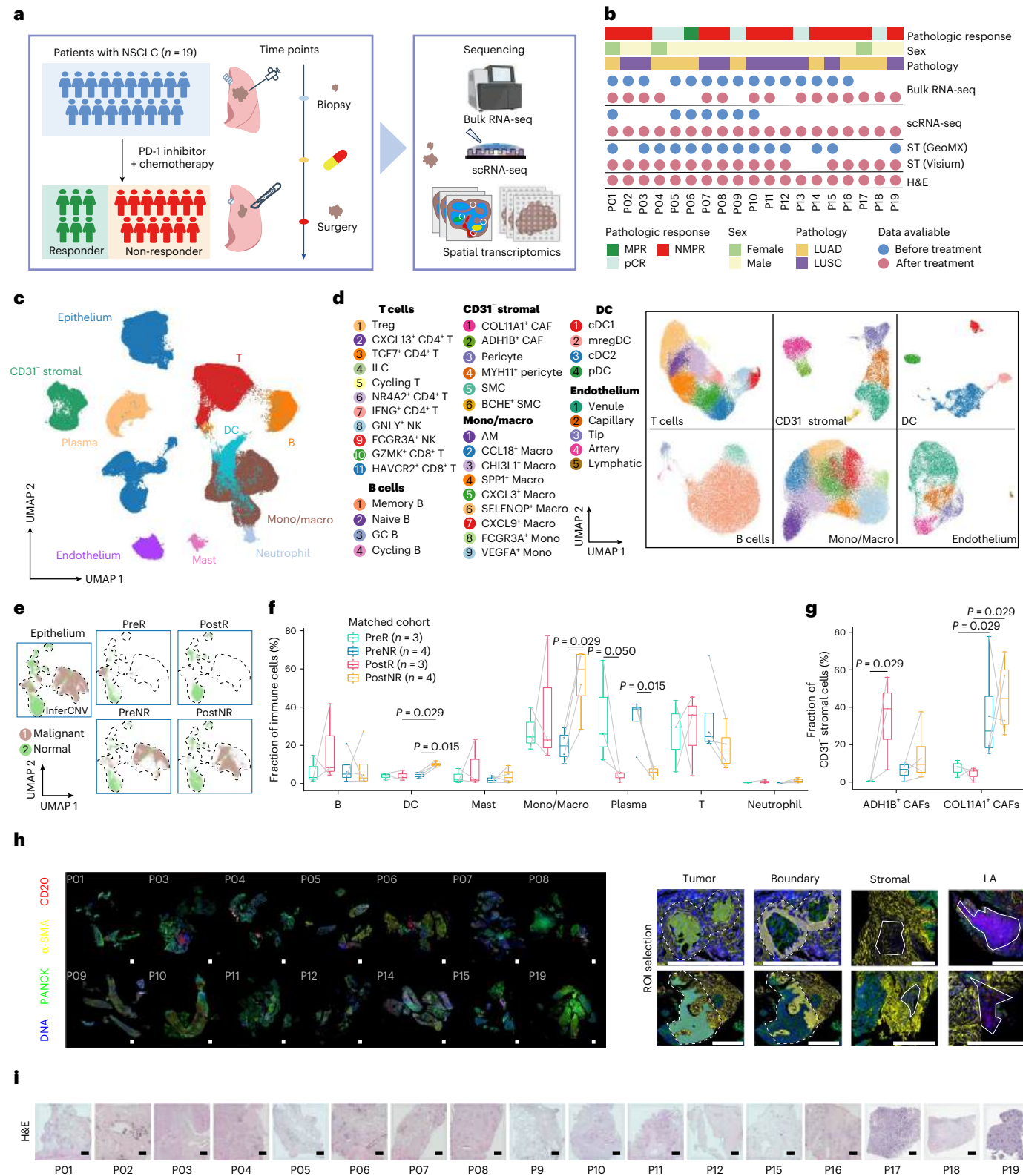
lineage in matched samples from three responders and four non-responders at baseline and post-treatment. A one-sided Wilcoxon test was used to determine statistical significance. **h**, Left, NanoString GeoMx DSP spatial transcriptomics analysis of specimens from the treatment-naïve cohort ($n = 14$). Right, selection of the ROIs: PANCK⁺ (tumor); α -SMA⁺ and adjacent tumor (boundary); α -SMA⁻ and far from tumor (stromal); and CD20⁺ (lymphocyte aggregation (LA)). Scale bars, 50 μ m. **i**, H&E staining of the specimens undergoing spatial transcriptomics using Visium (10x Genomics), from the cohort receiving immunotherapy ($n = 17$). Scale bars, 1 mm. AM, alveolar macrophage; cDC1/2 cell, conventional type 1/2 dendritic cells; GC, germinal center; ILC, innate lymphoid cells; LUSC, lung squamous cell carcinoma; LUAD, lung adenocarcinoma; mregDC, mature dendritic cell enriched in immunoregulatory molecules; NK, natural killer; pDC, plasmacytoid dendritic cell; PostNR, post-treatment non-responders; PostR, post-treatment responders; PreNR, pre-treatment non-responders; PreR, pre-treatment responders; SMC, smooth muscle cell; ST, spatial transcriptomics; T_{reg} cell, regulatory T cell. Panel **a** created with BioRender.com.

higher in pre-treatment non-responders compared with pre-treatment responders, whereas the IFNy score exhibited an opposite trend (Fig. 2e). This suggests that biological features of cancer cells may influence the clinical outcomes of immunotherapy. Using the DSP data, we examined pre-treatment tumor cell states. Similar to the cell state scores, the related genes of IFNy and NRF2 targets were significantly enriched in responders and non-responders, respectively (Fig. 2f,g). We further explored the spatial relationship between these two cell states

and other cell types (Fig. 2h). The IFNy score showed a positive correlation, whereas the NRF2 target score exhibited a negative correlation, with the proportion of adjacent immune cells (Fig. 2h,i). This suggests potential roles for cancer cell states in shaping the diverse TME.

Spatial maps of cellular compositions of NSCLC

To investigate the spatial organization and interactions of cellular components, we classified the post-treatment TME using Visium data.



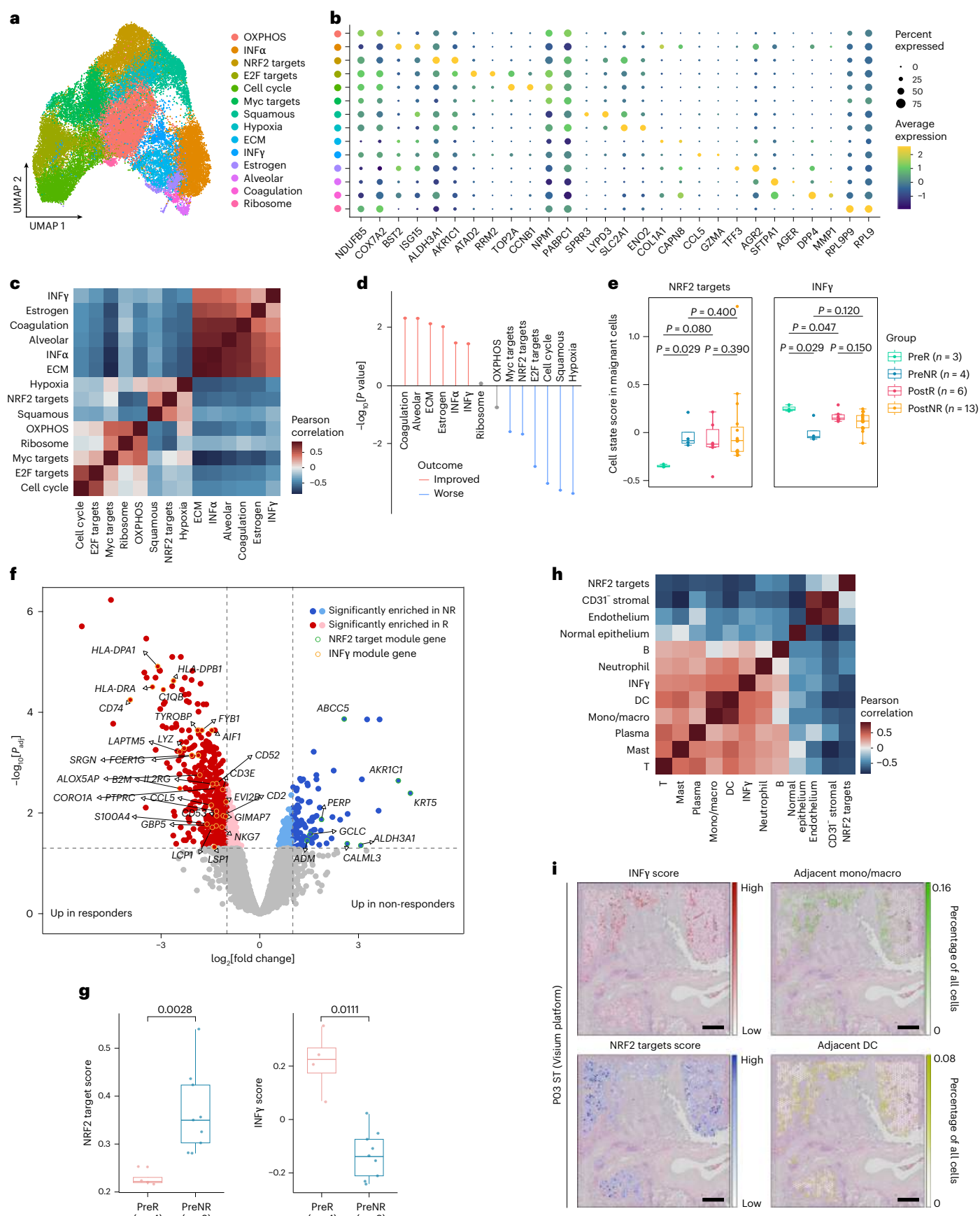


Fig. 2 | Cell states of cancer cells potentially define the response to ICB–chemotherapy.

a, UMAP plot showing cancer cells colored by cancer cell state. **b**, Dot plot displaying the average expression and expressed percentage of representative markers of each cancer cell state. **c**, Pearson's correlation of cancer cell state scores. **d**, Lollipop plot showing *P* values from Cox regression analysis linking cancer cell states to the clinical outcomes of patients from the TCGA-LUAD cohort. **e**, Boxplots showing the cell state scores for NRF2 targets (left) and IFN γ (right) in malignant cells from responders and non-responders during treatment. Sample numbers were as follows: $n = 3$ (PreR) $n = 4$ (PreNR), $n = 6$ (PostR) and $n = 13$ (PostNR). A one-sided Wilcoxon test was used to determine statistical significance. **f**, Volcano plot comparing responders' and non-responders' adjusted *P* values and fold changes across tumor ROIs.

A two-sided Wilcoxon test was used to determine statistical significance.

g, Boxplot showing the cell state scores for NRF2 targets (left) and IFN γ (right) in tumor ROIs from responders ($n = 4$) and non-responders ($n = 9$) before treatment using DSP data. A two-sided Wilcoxon test was used to determine statistical significance. **h**, Pearson's correlation of cell state scores (for NRF2 targets, IFN γ and adjacent cell types) across all malignant spots from Visium slides. **i**, Spatial distributions of IFN γ scores, NRF2 target scores and the abundances of adjacent monocytes/macrophages and dendritic cells in the TME of PO3. Scale bars, 1 mm. In **e** and **g**, center lines indicate median values and the lower and upper hinges represent 25th and 75th percentiles, respectively. The whiskers denote 1.5× the interquartile range. ECM, extracellular matrix; TNF, tumor necrosis factor.

Four distinct regions were classified based on hematoxylin and eosin (H&E) staining and definitions of tumor compartments from previous studies²²: tumor cores, invasive margins, isolated tumors and tumor stromal regions (Fig. 3a). As each spot from a Visium slide represents a mixture of cells, we performed cell type deconvolution analyses based on matched scRNA-seq data using STRIDE²³. Consistent with the H&E images, tumor cores were predominately occupied by malignant cells, whereas the invasive margins and isolated tumors contained both malignant and nonmalignant cells. There were almost no visible malignant cells in tumor stromal regions (Fig. 3a).

Unsupervised clustering of all spatial transcriptomics spots based on cell type composition identified 15 distinct cell type contexts (Fig. 3b). We hypothesized that these contexts represent potential spatial architecture that could be shared across patients, facilitating comparisons among different samples. We observed three malignancy-related cell type contexts (3, 10 and 13) and two fibroblastic cell type contexts (4 (enriched alcohol dehydrogenase 1B-positive (ADH1B $^+$) CAFs) and 8 (enriched COL11A1 $^+$ CAFs)), as well as four immune cell type contexts (1, 7, 9 and 12) (Fig. 3c,d and Extended Data Fig. 3a).

Spatial visualization of the contexts revealed valuable insights into their positional relationships and correlation with spatial architecture. For example, malignancy-related contexts 3 and 13 were surrounded by fibroblastic context 8, implying that tumor cells interact with fibroblasts at tumor boundaries (Fig. 3e). Additionally, the position of cell type context 9, enriched with germinal center B cells and CD4 $^+$ CXCL13 $^+$ T cells, corresponded to the position of lymphocyte aggregation (Fig. 3e and Extended Data Fig. 3a). These results provide additional insight into cellular compositions at tumor boundaries, as well as the spatial architectures of immune cells.

COL11A1 $^+$ CAFs exhibit a pro-tumor phenotype

Since COL11A1 $^+$ and ADH1B $^+$ CAFs showed different enrichment patterns in responders versus non-responders (Fig. 1g), we further explored the potential functions of the two distinct CAF subtypes. Previous studies categorized CAFs into two classes with different phenotypes in cancers: pro-tumor myofibroblastic CAFs (myCAFs) and inflammatory CAFs (iCAF) ²⁴. ADH1B $^+$ CAFs showed strong iCAF signatures and exhibited higher enrichment in tumor necrosis factor signaling and metabolic programs (Extended Data Fig. 4a,b).

Conversely, COL11A1 $^+$ CAFs were characterized by a pro-tumor myCAF phenotype, including heightened expression of extracellular matrix genes (*FAP*, *POSTN* and *CTHRC1*) and activated fibroblast markers

such as *GREMI* (Extended Data Figs. 2d and 4a). Gene set enrichment analysis revealed that gene signatures related to hypoxia, transforming growth factor beta (TGF β) signaling, epithelial-to-mesenchymal transition and angiogenesis were enriched in COL11A1 $^+$ CAFs (Extended Data Fig. 4b). Moreover, COL11A1 $^+$ CAFs also expressed *LRRC15*, closely resembling LRRC15 $^+$ CAFs reported to be induced by TGF β signaling in recent studies²⁵ (Extended Data Fig. 2d). NicheNet²⁶ analysis identified TGF β 1 as a predicted driver ligand for COL11A1 $^+$ CAFs (Extended Data Fig. 4c). TGF β has also been reported to promote tumorigenesis by shifting CAFs toward glycolysis²⁷, echoing the finding that COL11A1 $^+$ CAFs had higher glycolysis signature gene expression than ADH1B $^+$ CAFs (Extended Data Fig. 4b). Moreover, COL11A1 $^+$ CAFs differed from ADH1B $^+$ CAFs in the extracellular matrix program, as COL11A1 $^+$ CAFs specifically expressed genes encoding fibrillar collagens, including *COL10A1*, *COL11A1* and *COL12A1* (Extended Data Fig. 2d). We also noticed that the expression of *COL11A1* was significantly higher in non-responders before treatment (Extended Data Fig. 4d). Of the aforementioned collagen-encoding genes, *COL11A1* was associated with a worse prognosis in the TCGA-LUAD cohort²⁸ (Extended Data Fig. 4e). Overall, these findings suggest that ADH1B $^+$ CAFs exhibit an iCAF phenotype with specific metabolic programs, whereas COL11A1 $^+$ CAFs exhibit a pro-tumor myCAF phenotype.

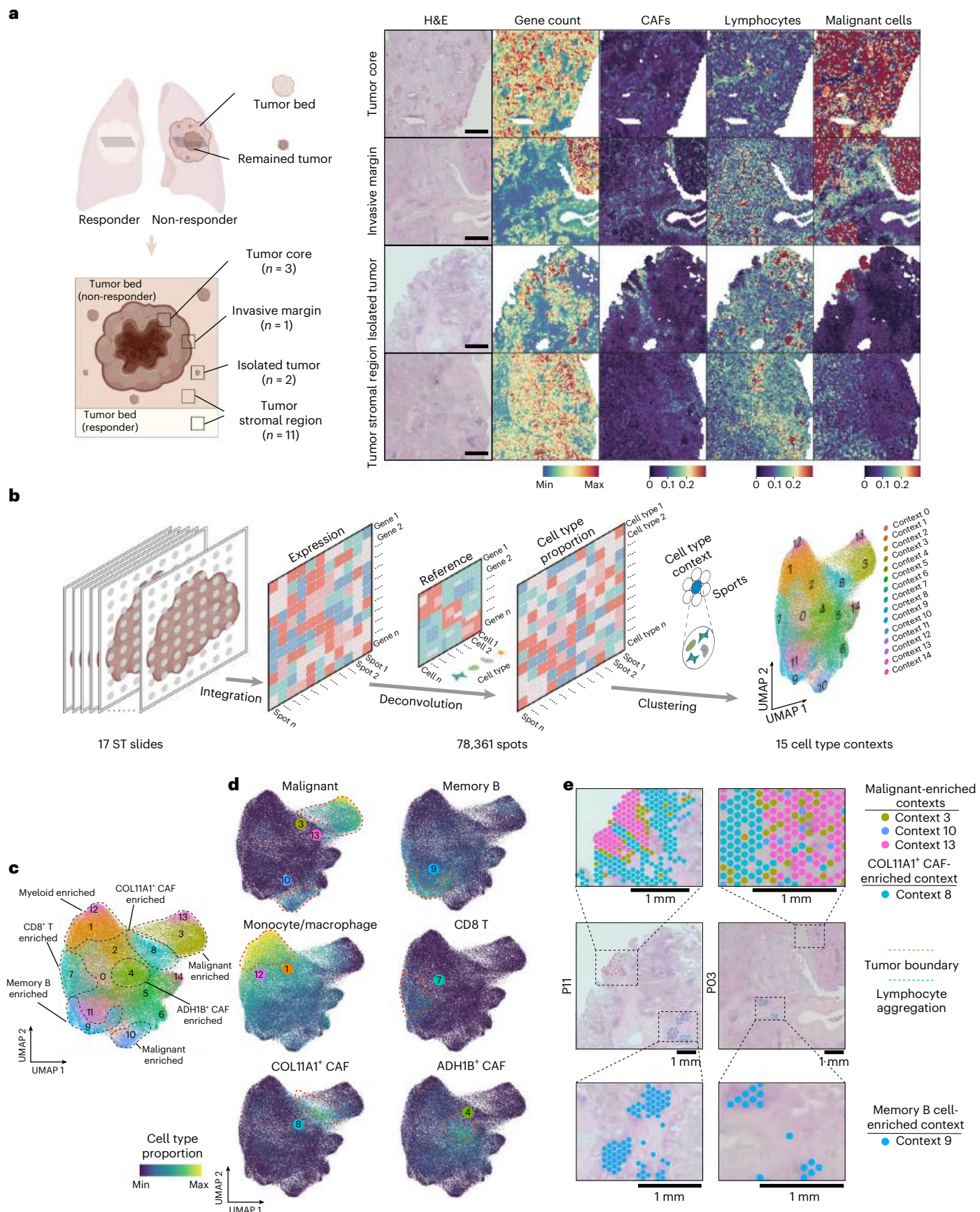
Accumulation of COL11A1 $^+$ CAFs at tumor boundaries

We compared the cell proportions at the tumor boundary before treatment between responders and non-responders. Non-responders exhibited a lower proportion of CD8 $^+$ T cells and a higher proportion of COL11A1 $^+$ CAFs than responders (Fig. 4a). Therefore, we hypothesized that COL11A1 $^+$ CAFs at tumor boundaries potentially block the infiltration of T cells. We further explored the spatial distribution of COL11A1 $^+$ CAFs and ADH1B $^+$ CAFs in tumor specimens. Interestingly, COL11A1 $^+$ CAFs aggregated at the boundaries of isolated tumors but dramatically decreased in the stromal regions far away from malignant cells in non-responders (Fig. 4b and Extended Data Fig. 4f-h). In tumor core regions and invasive margins, tumors were enveloped by COL11A1 $^+$ CAFs (Fig. 4c,d). Meanwhile, these COL11A1 $^+$ CAFs were nearly absent from tumor stromal regions in both responders and non-responders (Extended Data Fig. 4i). In contrast, ADH1B $^+$ CAFs were enriched in tumor stromal regions but absent at isolated tumor boundaries (Fig. 4b-d and Extended Data Fig. 4g,h). Consistently, there were hardly any ADH1B $^+$ CAFs in tumor core regions (Fig. 4c). Yet, ADH1B $^+$ CAFs were predominant in tumor stromal slides (Extended Data Fig. 4i).

Fig. 3 | Spatial cellular organization of NSCLC following ICB–chemotherapy.

a, Left, schematic of tissue sampling. Right, H&E staining, the distribution of gene counts and the abundance of CAFs, lymphocytes and malignant cells in spatial transcriptomics slides of four histologically defined categories: the tumor core ($n = 3$), invasive margin ($n = 1$), isolated tumor ($n = 2$) and tumor stromal regions ($n = 11$). Scale bars, 1 mm. **b**, Schematic of how the 15 cell type contexts were defined. **c**, UMAP of 15 types of spatial transcriptomics spot based on cell

type context. **d**, Highlighting of malignant cells, memory B cells, monocytes/macrophages, CD8 $^+$ T cells, COL11A1 $^+$ CAFs and ADH1B $^+$ CAFs based on the UMAP of cell type contexts. **e**, Spatial mapping of cell type contexts demonstrating the spatial distributions of three types of malignant cell context, the COL11A1 $^+$ CAF-enriched context and the memory B cell-enriched context. Scale bars, 1 mm. Panels **a** and **b** created with BioRender.com.



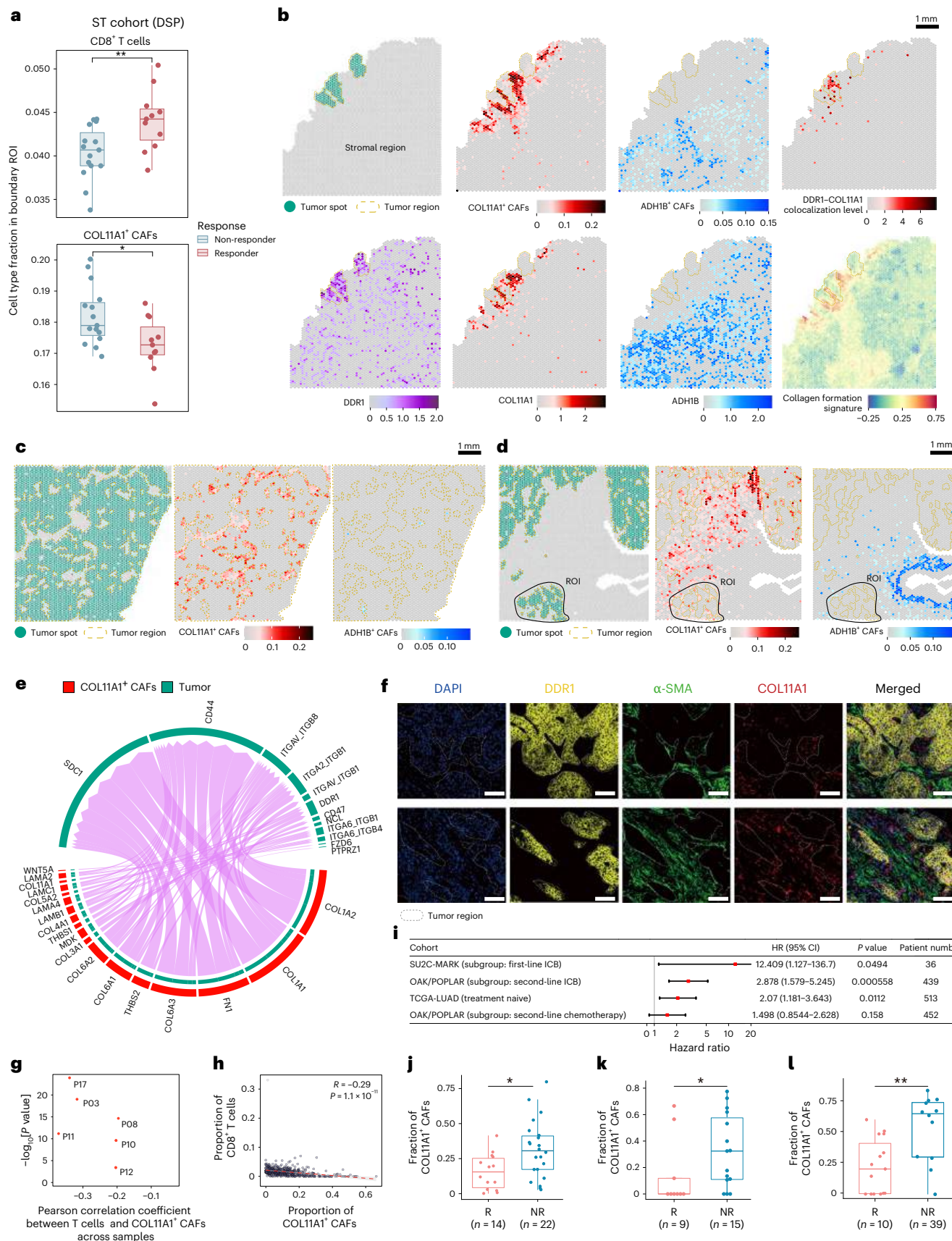


Fig. 4 | Spatial location and potential pro-carcinogenic function of COL11A1⁺ CAFs.

a, Boxplots showing the fractions of T cells and COL11A1⁺ CAFs in boundary ROIs from responders ($n = 11$) and non-responders ($n = 15$) pre-treatment. **b**, Spatial distributions of tumor spots, COL11A1⁺ CAFs and ADH1B⁺ CAFs, expression levels of DDR1, COL11A1 and ADH1B, colocalization levels of DDR1–COL11A1 and collagen formation signature scores in an isolated tumor sample from P11 (NMPR). The green dots and areas with green dashed borders represent tumor spots and tumor regions, respectively. **c**, Spatial distributions of tumor spots, COL11A1⁺ CAFs and ADH1B⁺ CAFs in a tumor core sample from P08 (NMPR). Note that ADH1B⁺ CAFs were devoid of tumor-rich regions. **d**, Spatial distributions of tumor spots, COL11A1⁺ CAFs and ADH1B⁺ CAFs in an invasive margin sample from P03 (NMPR). Scale bars in **b–d**, 1 mm. **e**, Cell-cell communication network between malignant cells and COL11A1⁺ CAFs in P11. **f**, Multiplex immunofluorescence staining showing the spatial locations of COL11A1⁺ fibroblasts (COL11A1⁺ and α -SMA⁺) and DDR1⁺ malignant cells in post-ICB–chemotherapy specimens. Scale bars, 100 μ m. **g**, Scatter plot showing the results of a Pearson's correlation test for the proportions of COL11A1⁺ CAFs and T cells near tumor cells in the Visium spatial transcriptomics cohort following ICB–chemotherapy. **h**, Scatter plot of the correlation between the proportion

of CD8⁺ T cells (calculated using the Estimating the Proportion of Immune and Cancer cells (EPIC) algorithm) and the proportion of COL11A1⁺ CAFs in the TCGA-LUAD cohort (treatment naïve). The red line represents the linear model and was fit using regression diagnostics. **i**, Forest plot of univariable Cox regression analysis for the NSCLC cohort studies. The red dots represent hazard ratios (HRs) of univariate Cox analysis. The black lines represent the 95% confidence interval (CI) for each hazard ratio. The P values were calculated using the Cox proportional model. **j**, Boxplot showing the fractions of COL11A1⁺ CAFs of responders ($R; n = 14$) and non-responders ($NR; n = 22$), estimated using CIBERSORTx, in the Stand Up To Cancer–Mark Foundation for Cancer Research subgroup cohort before ICB therapy. **k**, Boxplot showing the fractions of COL11A1⁺ CAFs of responders ($n = 9$) and non-responders ($n = 15$), estimated using CIBERSORTx, in an independent NSCLC cohort before ICB–chemotherapy. **l**, Boxplot showing the fractions of COL11A1⁺ CAFs among all fibroblasts in responders ($n = 10$) and non-responders ($n = 39$), estimated using CIBERSORTx, in a melanoma cohort ([GSE78220](#)) before ICB treatment. For the boxplots in **a** and **j–l**, the box limits denote the first and third quartiles, with the median shown in the center and the whiskers covering data within 1.5 \times the interquartile range from the box. * $P < 0.05$; ** $P < 0.01$.

The spatial relationship between COL11A1⁺ CAFs and cancer cells indicated their potential cell–cell interactions. Therefore, we performed cell–cell interaction analysis to identify potential interactions. The receptor-ligand interactions between discoidin domain receptor 1 (DDR1) and collagens (COL1A1, COL3A1, COL5A2 and COL11A1) were observed between tumor cells and COL11A1⁺ CAFs (Fig. 4e). Given that COL11A1 expression is specific to COL11A1⁺ CAFs (Extended Data Fig. 2d), we mainly focused on DDR1–COL11A1 colocalization for further analysis. The extracellular domain of DDR1 in tumors has been reported to facilitate collagen fiber alignment and to obstruct immune cell infiltration²⁹. Furthermore, the colocalization levels of DDR1–COL11A1, as well as collagen formation signatures, were highly enriched at tumor boundaries, yet declined in regions far away from cancer (Fig. 4b and Extended Data Fig. 4j). Immunofluorescence labeling also confirmed that COL11A1⁺ CAFs were located surrounding DDR1⁺ malignant cells in NSCLC following ICB–chemotherapy (Fig. 4f and Supplementary Note 4).

To explore whether COL11A1⁺ CAFs impede immune cell infiltration, we examined the association between COL11A1⁺ CAFs and T cells. The abundance of COL11A1⁺ CAFs around the spot containing malignant cells was observed to be significantly negatively correlated with the abundance of T cells in all samples containing malignant cells (Fig. 4g). Meanwhile, we found that T cell infiltration was also anticorrelated with the abundance of COL11A1⁺ CAFs in the treatment-naïve cohort (Fig. 4h).

We further assessed whether the abundance of COL11A1⁺ CAFs could be a reliable prognostic factor for NSCLC prognosis. The hazard

ratios for cohorts receiving ICB therapy were higher compared with those of treatment-naïve and chemotherapy cohorts^{30,31} (Fig. 4i), indicating that COL11A1⁺ CAFs might have played a more important role in the ICB therapy cohort. To further verify whether the abundance of COL11A1⁺ CAFs could predict the responsiveness to ICB therapy, we examined another two independent cohorts. The proportions of COL11A1⁺ CAFs were again significantly higher in non-responders than responders before ICB treatment (Fig. 4j,k). Interestingly, even in a melanoma cohort³², we observed similar trends (Fig. 4l). Altogether, the above analyses collectively indicated that COL11A1⁺ CAFs might be an effective biomarker for predicting prognosis and responsiveness to ICB therapy.

Secreted phosphoprotein 1-positive macrophages colocalize with COL11A1⁺ CAFs, blocking T cells

Previous studies have shown that CAF–macrophage interactions promote tumor growth in colon and liver cancers^{33,34}. We therefore explored the relationship between macrophages and COL11A1⁺ CAFs in NSCLC. We observed a positive correlation between the abundance of COL11A1⁺ CAFs and secreted phosphoprotein 1-positive (SPP1⁺) macrophages in scRNA-seq data (Fig. 5a). Consistent with the results for COL11A1⁺ CAFs (Fig. 1g), the fractions of SPP1⁺ macrophages were also significantly higher in non-responders both pre- and post-treatment (Fig. 5b and Extended Data Fig. 5a,b). Like COL11A1⁺ CAFs, SPP1⁺ macrophages also accumulated at tumor boundaries, showing a lower abundance and a dispersed distribution in stromal regions further away from the cancer (Fig. 5c–e and Extended Data Fig. 5c–e). Through

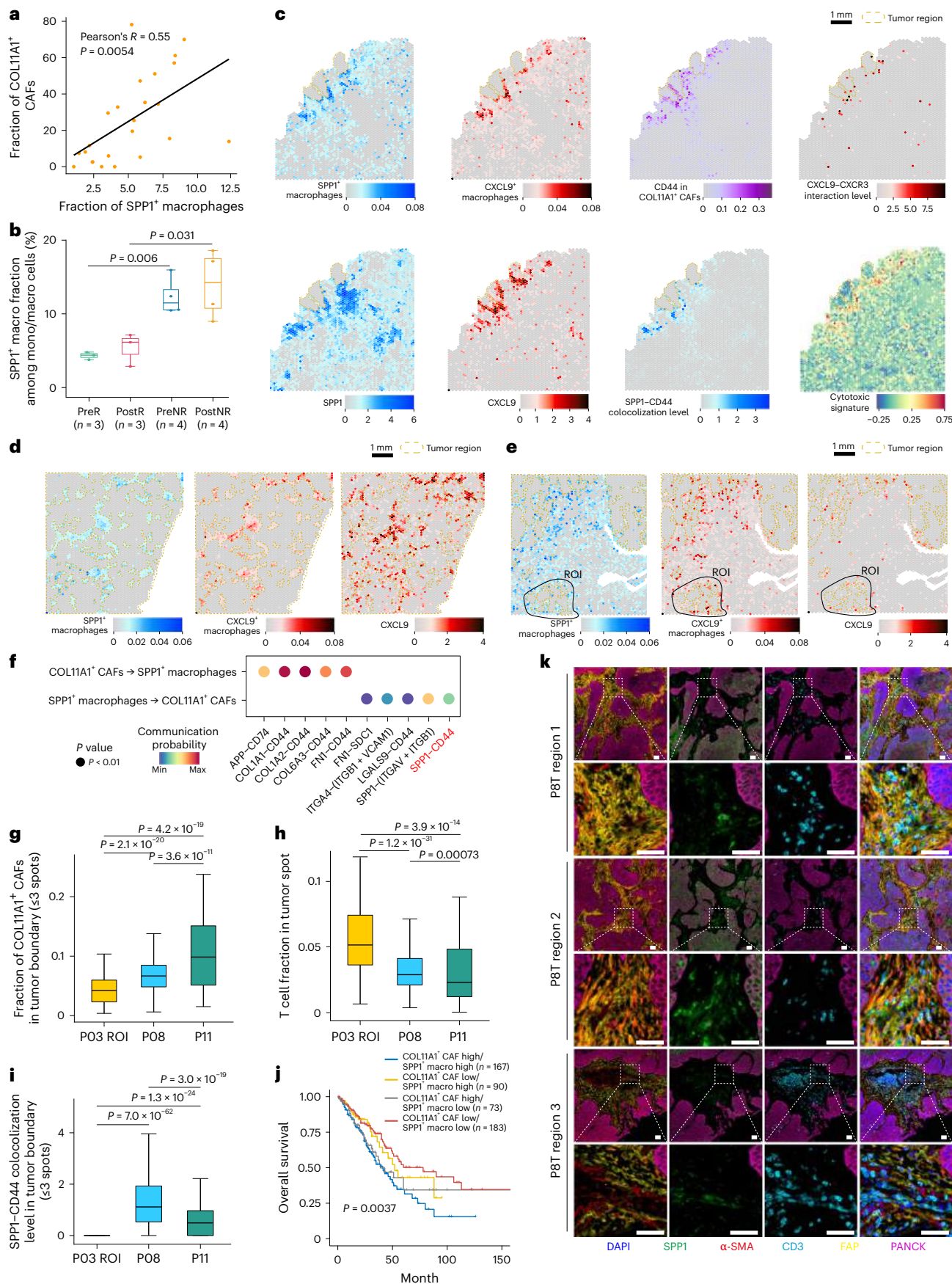
Fig. 5 | SPP1⁺ macrophages colocalize with COL11A1⁺ CAFs, blocking T cells.

a, Scatter plot showing a significant positive correlation between the fraction of COL11A1⁺ CAFs and the fraction of SPP1⁺ macrophages in single-cell samples. The black line represents the linear model and was fit using regression diagnostics after removing a hat value. **b**, Boxplot showing the fractions of SPP1⁺ macrophages in matched samples from three responders and four non-responders before and after treatment. A one-sided t -test was used to determine statistical significance. **c**, Spatial distributions of tumor spots, SPP1⁺ macrophages and CXCL9⁺ macrophages, COL11A1⁺ CAF-specific expression of CD44, expression of SPP1 and CXCL9 and colocalization levels between SPP1 and CD44 and between CXCL9 and CXCR3 in the slide of isolated tumor from P11 (NMPR). Cytotoxic signature scores for the same slide are included. **d**, Spatial distributions of tumor spots, SPP1⁺ macrophages and CXCL9⁺ macrophages and expression of CXCL9 in the slide of tumor core from P08 (NMPR). **e**, Spatial distributions of tumor spots, SPP1⁺ macrophages and CXCL9⁺ macrophages and expression of CXCL9 in the slide of invasive margin from P03. Scale bars in **c–e**, 1 mm. **f**, Cell-cell interactions between SPP1⁺ macrophages and COL11A1⁺

CAF in P08, inferred by CellChat, highlighting the SPP1–CD44 ligand–receptor pair (red text). Two-sided P values were determined by Student's t -test.

g–i, Boxplots comparing the fractions of COL11A1⁺ CAFs (**g**), fractions of T cells (**h**) and colocalization levels of SPP1–CD44 (**i**) at tumor boundaries (≤ 3 spots) from a COL11A1⁺ CAF-low region (P03 ROI; $n = 166$) and two COL11A1⁺ CAF-enriched regions (P08 ($n = 970$) and P11 ($n = 150$)). A two-sided Wilcoxon test was used to determine statistical significance. **j**, Kaplan–Meier survival curve for the TCGA-LUAD cohort, dichotomized by COL11A1⁺ CAF and SPP1⁺ macrophage signature scores. The survival curves were compared by log-rank test.

k, Multiplex immunofluorescence staining from another NSCLC sample (P8T) receiving ICB–chemotherapy, showing the spatial locations of COL11A1⁺ CAFs (α -SMA⁺ and fibroblast activation protein positive (FAP⁺)), SPP1⁺ macrophages (SPP1⁺ and PanCK⁻), T cells (CD3⁺) and tumor cells (PanCK⁺). Scale bars, 100 μ m. For the boxplots in **b** and **g–i**, the box limits denote the first and third quartiles, with the median shown in the center and the whiskers covering data within 1.5 \times the interquartile range from the box.



cell–cell interactions between SPP1⁺ macrophages and COL11A1⁺ CAFs, we noticed enrichment of the SPP1–CD44 pair (Fig. 5f). SPP1 secreted by macrophages promotes the proliferation and activation of CAFs and increases the deposition of collagen³⁵. Interestingly, the COL11A1⁺ CAF-low region, with a higher level of T cell infiltration, also had significantly lower colocalization levels of SPP1–CD44 compared with COL11A1⁺ CAF-high regions (Fig. 5g–i). This suggested that SPP1⁺ macrophages might cooperate with COL11A1⁺ CAFs to protect tumors from T cell infiltration. Patients exhibiting high levels of both COL11A1⁺ CAFs and SPP1⁺ macrophages consistently displayed the worst survival in the TCGA-LUAD cohort (Fig. 5j).

In addition, multiplex immunohistochemistry staining showed that SPP1⁺ macrophages (marked by SPP1) tended to localize at the tumor boundary with COL11A1⁺ CAFs (marked by alpha smooth muscle actin (α -SMA) and fibroblast activation protein; Extended Data Fig. 2d), whereas T cells (marked by CD3) were blocked by the combination of these two cell types (Fig. 5k and Supplementary Note 4). Moreover, CXCL9⁺ macrophages and cytotoxic immune cells failed to enter tumor beds in the presence of COL11A1⁺ CAFs (Supplementary Note 1).

Together, these results indicate that the formation of the tumor boundary structure associated with SPP1⁺ macrophages and COL11A1⁺ CAFs might contribute to the immunosuppressive microenvironment of NSCLC.

Comprehensive assessment of TLS maturation and recession

TLSs were prevalent in the TME of NSCLC after ICB–chemotherapy (see Supplementary Note 2). Several studies have reported that TLSs in the TME follow sequential maturation stages^{36,37}. The genesis of TLSs is believed to start from the local production of cytokines such as interleukin-7, which recruit lymphoid tissue inducer (LTi) cells to the site of inflammation. Then, LTi cells interact with stromal cells through the lymphotxin $\alpha_1\beta_2$ –LT β receptor signaling pathway to initiate the formation of TLSs¹². Interestingly, although TLSs were present in most samples, spatial distributions of LT β –LT β receptor signal were only detected in a few slides (Extended Data Fig. 8a). We therefore speculated that the apparent heterogeneity of TLSs across samples might reflect different maturation stages of TLSs. To comprehensively characterize the maturation process of TLSs, we gathered TLSs from all samples and projected them onto the same low-dimension space (Fig. 6a). Genes encoding TLS-initiating markers (*RORC* and *IL7R*) were indeed enriched in similar distributions, whereas those encoding functional cytokines (*LTB* and *CXCL13*) were enriched in different subsets of TLSs (Fig. 6b). K-means clustering was utilized to distinguish the different maturation stages of TLSs (Fig. 6c), which included early lymphoid aggregates (featured by high expression of LTi markers and low cytokine expression), activated TLSs (high cytokine expression),

declining TLSs (decreased cytokine expression) and late TLSs (very low cytokine expression) (Fig. 6c).

We further investigated the immune cell subtype compositions of TLSs at different stages (Fig. 6d, Extended Data Fig. 8b and Supplementary Note 3). These results collectively suggested that germinal center B cells, effector memory CD4 T cells and follicular helper T cells are important for the activation and function of TLSs, whereas memory B cells are more related to the long-term effects of TLSs.

To explore the relationship between TLS maturation and responsiveness to ICB–chemotherapy, we visualized the distribution of TLSs in different states in each specimen. The maturation stages showed remarkable diversity among patients, and even within the same slide (Fig. 6e,f). In non-responders, the trend that more TLSs were detected with a decrease in the residual tumor load after immunotherapy implied potential anti-tumor roles of TLSs (Fig. 6e). In the non-pCR group, patients with activated TLSs had lower residual tumor fractions (Fig. 6g), indicating that activated TLSs are associated with better prognosis¹⁴. Surprisingly, in contrast with non-responders, patients with a pCR had fewer TLSs, with almost all of them in the late stage (Fig. 6e). These findings potentially suggest a state of recessed immune response in the TMEs of responders. Moreover, the different maturation states of TLSs displayed distinct position biases. In particular, the majority of intratumoral TLSs belonged to the early lymphoid aggregate state, whereas recessionary TLSs were closer to residual tumor cells compared with activated TLSs (Fig. 6f), implying the possibility of an immunosuppressive environment in the vicinity of tumor cells.

TLS maturation correlates with clinical outcome in NSCLC

The analyses above suggest that the maturation statuses of TLSs are highly heterogeneous among patients with different responses. We further examined differences between responders' and non-responders' TLSs in the same state. Given that almost all TLSs observed in patients with a pCR were at the late stage, we performed a differential expression analysis of late TLSs in patients with a pCR versus an NMPR. Compared with those in responders, the late TLSs in non-responders expressed higher levels of *HIF1A* and *ENO1*, which have been reported to be involved in the response to hypoxia and process of glycolysis, respectively (Fig. 6h and Supplementary Table 3). In addition, genes encoding heat shock proteins, such as *HSP90B1* and *HSP90AA1*, were highly expressed in the late TLSs of non-responders (Fig. 6h). Considering heat shock proteins are usually upregulated under different stress conditions, including hypoxia³⁸, we conjectured that the late TLSs of non-responders were under a hypoxic environment. Further functional analyses revealed the enrichment of pathways related to glycolysis and hypoxia response in late TLSs of non-responders as well (Fig. 6i and Extended Data Fig. 8c). Interestingly, no highly expressed genes were

Fig. 6 | Characteristics of TLSs at different stages, and clinical significance of TLSs. **a**, PCA visualization of all TLSs from all samples. **b**, PCA visualization of the expression of TLS-related marker genes. **c**, PCA visualization of k-means clustering and annotation of all TLSs. **d**, Heatmaps showing the enrichment of B (left) and T cell (right) subtypes in different TLS states. **e**, Distribution of TLSs in different states in all samples. **f**, Spatial distributions of TLSs at different stages in tumor samples from three non-responders. Scale bars, 1 mm. **g**, Boxplot showing the difference in residual tumor fractions between patients with and without activated TLSs in the non-pCR group. **h**, Volcano plot showing the differentially expressed genes in late TLSs from the NMPR group versus those from the pCR group. Two-sided Wilcoxon rank sum test was used to determine the statistical significance. **i**, Bar plot showing the enriched Gene Ontology-biological process (GO-BP) pathways of significantly elevated genes in TLSs from NMPR as compared to those from pCR. The color represents the significance. A Fisher's exact test was used to determine two-sided P values, denoting the enrichment P values of the pathway IDs. **j**, Boxplot showing the distributions of hypoxia signature scores of TLSs in different states: lymphoid aggregates ($n = 42$), activated TLSs ($n = 71$), declining TLSs ($n = 103$), late TLSs (pCR) ($n = 26$)

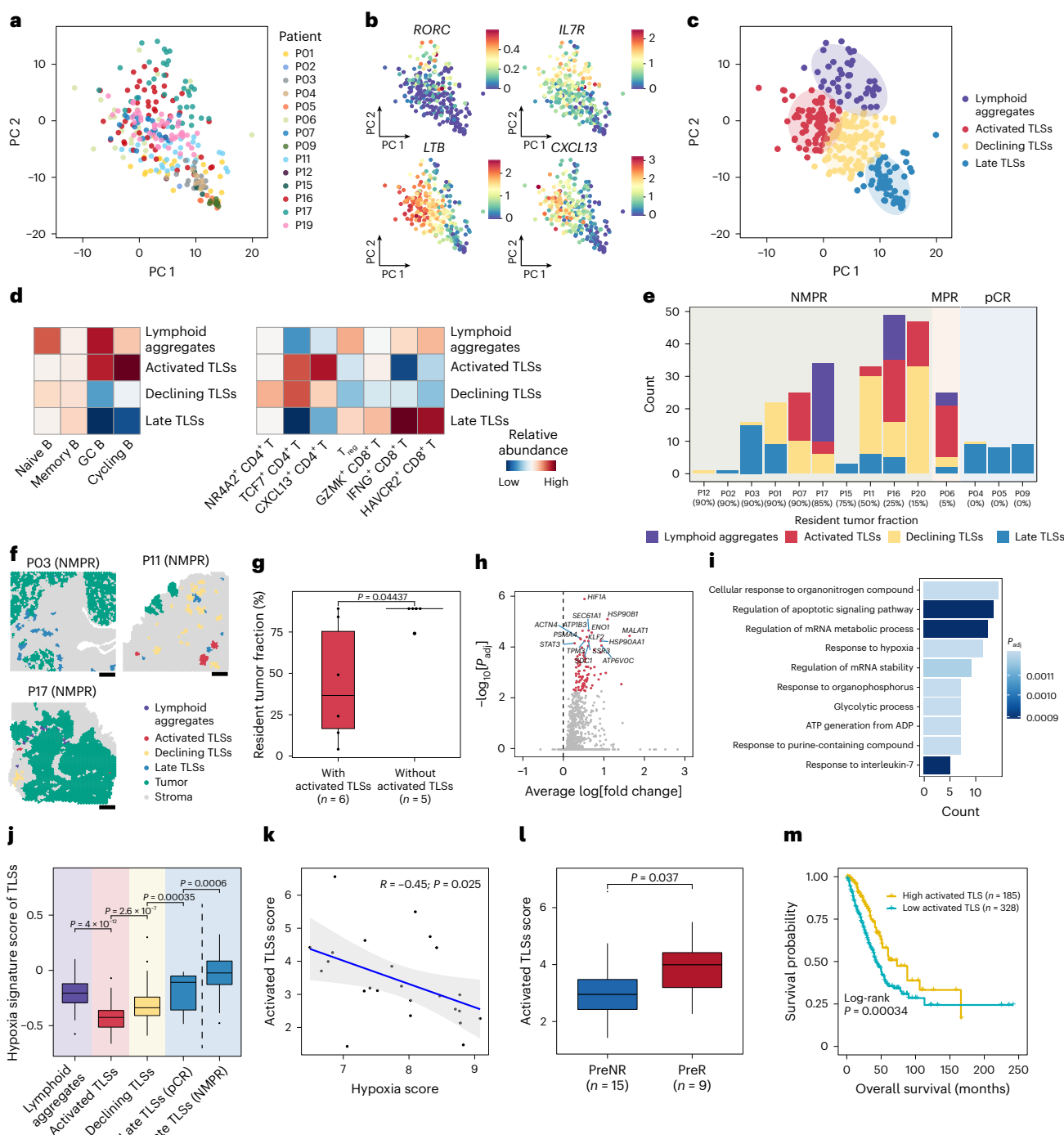
and late TLSs (NMPR) ($n = 39$). A two-sided Wilcoxon rank-sum test was used to determine statistical significance. **k**, Correlation between activated TLS score and hypoxia signature score in another pre-treatment NSCLC cohort, measured by bulk RNA-seq. The blue line represents the regression line. The gray band is the 95% confidence interval for the regression line. Each scattered dot represents a sample from the cohort. The TLS and hypoxia scores were defined as the average expression of corresponding signature genes from Supplementary Table 4. The two-sided P value was determined by Pearson's correlation test. **l**, Boxplot showing activated TLS signature scores before ICB–chemotherapy in non-responders (preNR; $n = 15$) and responders (preR; $n = 9$) from another independent NSCLC cohort, measured by bulk RNA-seq. A one-sided Wilcoxon rank-sum test was used to determine statistical significance. **m**, Kaplan–Meier survival curve for the TCGA-LUAD cohort, dichotomized by activated TLS signature. Statistical significance was determined by log-rank test. For the boxplots in **g**, **j** and **l**, the box limits denote the first and third quartiles, with the median shown in the center and the whiskers covering data within 1.5× the interquartile range from the box. mRNA, messenger RNA.

identified in the late TLSs of patients with a pCR (Fig. 6h), suggesting a recessionary and quiescent state of these TLSs. Collectively, these results indicate that late TLSs of non-responders located in a hypoxic TME might be unfavorable for maintaining functional TLSs.

Interestingly, increased hypoxia signature scores were also associated with early-stage TLSs of non-responders following ICB-chemotherapy (Fig. 6j and Extended Data Fig. 8d). Previous studies have reported that hypoxia could cause enhancement of regulatory T cells in the TME^{39,40}, consistent with the enrichment of regulatory T cells in the lymphoid aggregate state (Fig. 6d and Extended Data Fig. 8b). Another study discovered that hypoxia could enhance immunosuppression by inhibiting CD4 effector T cells⁴¹. Indeed, we observed that the hypoxia signature score in TLSs was positively correlated with the fraction of regulatory T cells and negatively correlated with

effector memory CD4 T cells (Extended Data Fig. 8e). We therefore speculated that hypoxia might create an immunosuppressive TME, thus suppressing TLS activation. To examine this, we calculated the correlation between the hypoxia score and TLS activation score in another NSCLC cohort. The overall negative correlation between these two scores implied that the hypoxic TME might have an inhibitory impact on TLS formation (Fig. 6k). Altogether, these results suggest that a hypoxic TME could promote regulatory T cell infiltration and inhibit CD4 effector memory T cells to suppress the formation and maintenance of TLSs.

Furthermore, we also investigated the potential of TLS maturation status as a predictor of patient survival and response to ICB-chemotherapy. Most of the TLSs in the patients with an MPR were identified as activated TLSs using the spatial transcriptomics data,



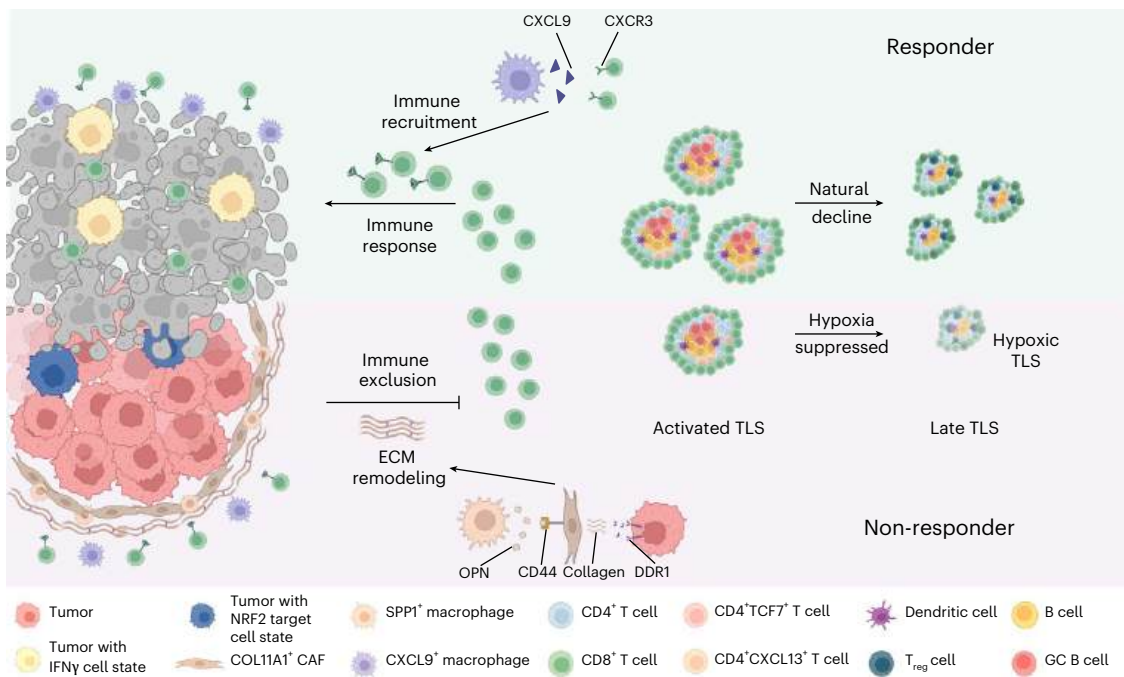


Fig. 7 | Summary of this study. Schematic of the TME compartmentalization of NSCLC after ICB-chemotherapy in responders and non-responders. OPN, osteopontin, encoded by the SPP1. Created with BioRender.com.

whereas in the non-pCR group, patients with activated TLSs had lower percentages of residual tumor (Fig. 6e,g). Another independent NSCLC cohort also showed that the activated TLS signature was significantly higher in responders than non-responders at baseline (Fig. 6l). Additionally, a higher activated TLS signature was associated with better overall survival in TCGA-LUAD cohort patients (Fig. 6m). In brief, our analyses suggest that activated TLSs are beneficial for patient survival and might serve as a potential biomarker or therapeutic target for future immunotherapy.

Discussion

In this study, we delved into the transcriptional characteristics associated with resistance to ICB combined with chemotherapy in NSCLC by utilizing spatial transcriptomics and single-cell sequencing technology (Fig. 7).

Evidence has been accumulating on how cancer cell state plasticity impacts cancer evolution and clinical outcomes^{42,43}. In cervical squamous cell carcinoma, specific cancer cell states shape the TME and clinical outcomes⁴⁴. In this study, we identified 14 distinct cancer cell states in NSCLC samples. Tumor cell states associated with NRF2 targets and IFNy in treatment-naïve samples were linked to poor and favorable responses to ICB-chemotherapy, respectively. NRF2 activation has been reported to promote lung cancer tumorigenesis⁴⁵, accounts for multidrug resistance and is associated with poor prognosis^{46,47}. Activation of the NRF2 pathway is associated with less CD3⁺CD8⁺T cell infiltration into tumor beds⁴⁸. Consistently, the NRF2 target cell state score was negatively correlated with immune infiltration in our data. This finding underscores the significance of NRF2 pathway activation as a potential resistance factor that may disrupt tumor-immune interactions in response to ICB-chemotherapy in NSCLC. In contrast, the proinflammatory IFNy pathway could be involved in promoting cytotoxic immune cell infiltration and cancer elimination, leading to good prognosis.

The TME contains heterogeneous populations of fibroblasts with both tumor-promoting and suppressive roles^{49–52}. The targeting of CAFs has been considered an effective way of enhancing ICB therapeutic efficacy in pre-clinical models^{53–55}. In our study, we identified that

COL11A1⁺ CAFs were significantly more abundant in non-responders than responders. Interestingly, we observed that COL11A1⁺ CAFs were predominantly localized at tumor boundary regions after ICB-chemotherapy, which could potentially block the contact between tumor cells and cytotoxic immune cells. We observed that collagen produced by COL11A1⁺ CAFs might interact with the tumor cell-surface receptor DDR1 at tumor boundaries. DDR1 has been reported to promote collagen fiber alignment to enhance tumor immune exclusion²⁹. These results highlight common mechanisms for immune exclusion achieved by CAFs and suggest that COL11A1⁺ CAFs are a potential pan-cancer therapeutic target. Additionally, SPP1⁺ macrophages were present in the fibroblast compartment, which may promote collagen secretion by COL11A1⁺ CAFs through SPP1-CD44 interaction. Thus, blocking this interaction may represent an effective regimen by which to overcome immunotherapy resistance caused by CAF. However, CD44 is widely expressed in multiple cell lineages and navigating CD44 inhibitors to antagonize CD44 in CAFs is challenging. In contrast, SPP1 is selectively expressed in tumor-associated macrophages and tumor cells⁵⁶ and has been reported to regulate colony stimulating factor 1 to recruit myeloid-derived suppressive cells into the TME⁵⁷. Therefore, inhibition of SPP1 may confer a two birds, one stone benefit. A previous study reported that WDR5 inhibitors could reduce the expression of SPP1 by suppressing H3K4me3 in tumor cells and tumor-associated macrophages⁵⁶. Although these WDR5 inhibitors have not been tested in a clinical setting, our study suggests that assessing their safety and efficacy in future clinical studies to treat NSCLC is plausible.

The colocalization of CD4 T and B cells indicated the prevalent presence of TLSs and this was validated by pathological examination. TLSs have been found in various cancer types and have been linked to favorable outcomes following ICB treatment in melanoma, sarcoma and renal cell carcinoma^{13,58,59}. Using tissue morphologies from H&E images and transcriptome features from spatial transcriptomics, we systematically evaluated the potential TLS maturation process in NSCLC TMEs. Our analyses identified four different stages of TLSs, which were in general comparable to the previous classification as early TLSs (lymphoid aggregates), primary follicular-like TLSs (with follicular dendritic cells but lacking germinal centers) and secondary

follicular-like TLSs (containing both follicular dendritic cells and germinal centers)^{36,37}. In addition, we defined a late-stage TLS as featuring low cytokine expression. Intriguingly, late TLSs exhibited differential states in responders and non-responders. Responders showed a quiescent state of late TLSs, possibly due to a lack of persistent tumor antigenic stimulation. In contrast, in non-responders, late TLSs and early lymphoid aggregates were in an immunosuppressive hypoxic state this may have suppressed both TLS formation and maintenance. It remains possible that in non-responders some lymphoid aggregate TLSs can never become mature and remain in an immature state due to suppression from the hypoxic environment⁶⁰. The underlying regulatory mechanisms of hypoxia in TLS activation and suppression need to be further clarified by combining in vitro and in vivo perturbation experiments together with higher-resolution spatiotemporal analyses. Notably, our findings suggest that the evaluation of TLS status may have prognostic value for patients with NSCLC undergoing immunotherapy and could inform treatment decisions and patient management strategies.

In summary, our study provides a high-resolution spatial cellular and molecular atlas of the TME in NSCLC before and after neoadjuvant ICB–chemotherapy. Using single-cell and spatial transcriptomic analyses, we identified distinct tumor cell features and microenvironment compartments that displayed remarkable heterogeneity and dynamic changes in response to treatment. These results highlight the potential of therapies that target multiple components of the TME, including fibroblasts, macrophages and TLSs, and suggest new avenues for developing combinatorial therapies.

Online content

Any methods, additional references, Nature Portfolio reporting summaries, source data, extended data, supplementary information, acknowledgements, peer review information; details of author contributions and competing interests; and statements of data and code availability are available at <https://doi.org/10.1038/s41588-024-01998-y>.

References

1. Brahmer, J. et al. Nivolumab versus docetaxel in advanced squamous-cell non-small-cell lung cancer. *N. Engl. J. Med.* **373**, 123–135 (2015).
2. Socinski, M. A. et al. Atezolizumab for first-line treatment of metastatic nonsquamous NSCLC. *N. Engl. J. Med.* **378**, 2288–2301 (2018).
3. Bian, D. L. et al. Neoadjuvant Afatinib for stage III EGFR-mutant non-small cell lung cancer: a phase II study. *Nat. Commun.* **14**, 4655 (2023).
4. Lu, S. et al. Perioperative toripalimab plus chemotherapy for patients with resectable non-small cell lung cancer: the Neotorch Randomized Clinical Trial. *J. Am. Med. Assoc.* **331**, 201–211 (2024).
5. Xia, H. R. et al. Neoadjuvant camrelizumab (an anti-PD-1 antibody) plus chemotherapy or apatinib (a VEGFR-2 inhibitor) for initially unresectable stage II–III non-small-cell lung cancer: a multicentre, two-arm, phase 2 exploratory study. *Signal Transduct. Target. Ther.* **9**, 145 (2024).
6. Zhu, X. et al. Safety and effectiveness of neoadjuvant PD-1 inhibitor (toripalimab) plus chemotherapy in stage II–III NSCLC (LungMate 002): an open-label, single-arm, phase 2 trial. *BMC Med.* **20**, 493 (2022).
7. Jia, X. H. et al. Efficacy and safety of neoadjuvant immunotherapy in resectable nonsmall cell lung cancer: a meta-analysis. *Lung Cancer* **147**, 143–153 (2020).
8. Quail, D. F. & Joyce, J. A. Microenvironmental regulation of tumor progression and metastasis. *Nat. Med.* **19**, 1423–1437 (2013).
9. Caushi, J. X. et al. Transcriptional programs of neoantigen-specific TIL in anti-PD-1-treated lung cancers. *Nature* **596**, 126–132 (2021).
10. Liu, B. L. et al. Temporal single-cell tracing reveals clonal revival and expansion of precursor exhausted T cells during anti-PD-1 therapy in lung cancer. *Nat. Cancer* **3**, 108–121 (2022).
11. Sautès-Fridman, C. et al. Tertiary lymphoid structures in cancers: prognostic value, regulation, and manipulation for therapeutic intervention. *Front. Immunol.* **7**, 407 (2016).
12. Sautès-Fridman, C., Petitprez, F., Calderaro, J. & Fridman, W. H. Tertiary lymphoid structures in the era of cancer immunotherapy. *Nat. Rev. Cancer* **19**, 307–325 (2019).
13. Petitprez, F. et al. B cells are associated with survival and immunotherapy response in sarcoma. *Nature* **577**, 556–560 (2020).
14. Vanhersecke, L. et al. Mature tertiary lymphoid structures predict immune checkpoint inhibitor efficacy in solid tumors independently of PD-L1 expression. *Nat. Cancer* **2**, 794–802 (2021).
15. Travis, W. D. et al. IASLC multidisciplinary recommendations for pathologic assessment of lung cancer resection specimens after neoadjuvant therapy. *J. Thorac. Oncol.* **15**, 709–740 (2020).
16. William, W. N. et al. Computed tomography RECIST assessment of histopathologic response and prediction of survival in patients with resectable non-small-cell lung cancer after neoadjuvant chemotherapy. *J. Thorac. Oncol.* **8**, 222–228 (2013).
17. Patel, A. P. et al. Single-cell RNA-seq highlights intratumoral heterogeneity in primary glioblastoma. *Science* **344**, 1396–1401 (2014).
18. Barkley, D. et al. Cancer cell states recur across tumor types and form specific interactions with the tumor microenvironment. *Nat. Genet.* **54**, 1192–1201 (2022).
19. Neftel, C. et al. An integrative model of cellular states, plasticity, and genetics for glioblastoma. *Cell* **178**, 835–849.e21 (2019).
20. Puram, S. V. et al. Single-cell transcriptomic analysis of primary and metastatic tumor ecosystems in head and neck cancer. *Cell* **171**, 1611–1624.e24 (2017).
21. Tirosi, I. et al. Single-cell RNA-seq supports a developmental hierarchy in human oligodendrogloma. *Nature* **539**, 309–313 (2016).
22. Fu, T. et al. Spatial architecture of the immune microenvironment orchestrates tumor immunity and therapeutic response. *J. Hematol. Oncol.* **14**, 98 (2021).
23. Sun, D. Q., Liu, Z. Y., Li, T. W., Wu, Q. & Wang, C. F. STRIDE: accurately decomposing and integrating spatial transcriptomics using single-cell RNA sequencing. *Nucleic Acids Res.* **50**, e42 (2022).
24. Ohlund, D. et al. Distinct populations of inflammatory fibroblasts and myofibroblasts in pancreatic cancer. *J. Exp. Med.* **214**, 579–596 (2017).
25. Krishnamurty, A. T. et al. LRRC15⁺ myofibroblasts dictate the stromal setpoint to suppress tumour immunity. *Nature* **611**, 148–154 (2022).
26. Browaeys, R., Saelens, W. & Saeys, Y. NicheNet: modeling intercellular communication by linking ligands to target genes. *Nat. Methods* **17**, 159–162 (2020).
27. Guido, C. et al. Metabolic reprogramming of cancer-associated fibroblasts by TGF-β drives tumor growth: connecting TGF-β signaling with “Warburg-like” cancer metabolism and L-lactate production. *Cell Cycle* **11**, 3019–3035 (2012).
28. Weinstein, J. N. et al. The Cancer Genome Atlas Pan-Cancer analysis project. *Nat. Genet.* **45**, 1113–1120 (2013).
29. Sun, X. J. et al. Tumour DDR1 promotes collagen fibre alignment to instigate immune exclusion. *Nature* **599**, 673–678 (2021).
30. Patil, N. S. et al. Intratumoral plasma cells predict outcomes to PD-1 blockade in non-small cell lung cancer. *Cancer Cell* **40**, 289–300.e4 (2022).
31. Ravi, A. et al. Genomic and transcriptomic analysis of checkpoint blockade response in advanced non-small cell lung cancer. *Nat. Genet.* **55**, 807–819 (2023).

32. Hugo, W. et al. Genomic and transcriptomic features of response to anti-PD-1 therapy in metastatic melanoma. *Cell* **165**, 35–44 (2016).
33. Qi, J. J. et al. Single-cell and spatial analysis reveal interaction of FAP⁺ fibroblasts and SPP1⁺ macrophages in colorectal cancer. *Nat. Commun.* **13**, 1742 (2022).
34. Sathe, A. et al. Colorectal cancer metastases in the liver establish immunosuppressive spatial networking between tumor-associated SPP1⁺ macrophages and fibroblasts. *Clin. Cancer Res.* **29**, 244–260 (2023).
35. Chen, S. Q. et al. β -catenin-controlled tubular cell-derived exosomes play a key role in fibroblast activation via the OPN–CD44 axis. *J. Extracell. Vesicles* **11**, e12203 (2022).
36. Silina, K. et al. Germinal centers determine the prognostic relevance of tertiary lymphoid structures and are impaired by corticosteroids in lung squamous cell carcinoma. *Cancer Res.* **78**, 1308–1320 (2018).
37. Posch, F. et al. Maturation of tertiary lymphoid structures and recurrence of stage II and III colorectal cancer. *Oncolmumonology* **7**, e1378844 (2018).
38. Baird, N. A., Turnbull, D. W. & Johnson, E. A. Induction of the heat shock pathway during hypoxia requires regulation of heat shock factor by hypoxia-inducible factor-1. *J. Biol. Chem.* **281**, 38675–38681 (2006).
39. Facciabene, A. et al. Tumour hypoxia promotes tolerance and angiogenesis via CCL28 and T_{reg} cells. *Nature* **475**, 226–230 (2011).
40. Ren, L. et al. Hypoxia-induced CCL28 promotes recruitment of regulatory T cells and tumor growth in liver cancer. *Oncotarget* **7**, 75763–75773 (2016).
41. Westendorf, A. M. et al. Hypoxia enhances immunosuppression by inhibiting CD4⁺ effector T cell function and promoting T_{reg} activity. *Cell. Physiol. Biochem.* **41**, 1271–1284 (2017).
42. Da Silva-Diz, V., Lorenzo-Sanz, L., Bernat-Peguera, A., Lopez-Cerda, M. & Munoz, P. Cancer cell plasticity: impact on tumor progression and therapy response. *Semin. Cancer Biol.* **53**, 48–58 (2018).
43. Qin, S. et al. Emerging role of tumor cell plasticity in modifying therapeutic response. *Signal Transduct. Target. Ther.* **5**, 1995–2030 (2020).
44. Fan, J. et al. Multiomic analysis of cervical squamous cell carcinoma identifies cellular ecosystems with biological and clinical relevance. *Nat. Genet.* **55**, 2175–2188 (2023).
45. Singh, A. et al. NRF2 activation promotes aggressive lung cancer and associates with poor clinical outcomes. *Clin. Cancer Res.* **27**, 877–888 (2021).
46. Jeong, Y. et al. Role of KEAP1/NFE2L2 mutations in the chemotherapeutic response of patients with non-small cell lung cancer. *Clin. Cancer Res.* **26**, 274–281 (2020).
47. Kralj, E. B. et al. KEAP1 loss modulates sensitivity to kinase targeted therapy in lung cancer. *eLife* **6**, e18970 (2017).
48. Duan, J. et al. Tumor-immune microenvironment and NRF2 associate with clinical efficacy of PD-1 blockade combined with chemotherapy in lung squamous cell carcinoma. *Cell Rep. Med.* **4**, 101302 (2023).
49. Sugimoto, H., Mundel, T. M., Kieran, M. W. & Kalluri, R. Identification of fibroblast heterogeneity in the tumor microenvironment. *Cancer Biol. Ther.* **5**, 1640–1646 (2006).
50. Ozdemir, B. C. et al. Depletion of carcinoma-associated fibroblasts and fibrosis induces immunosuppression and accelerates pancreas cancer with reduced survival. *Cancer Cell* **25**, 719–734 (2014).
51. Ohlund, D., Elyada, E. & Tuveson, D. Fibroblast heterogeneity in the cancer wound. *J. Exp. Med.* **211**, 1503–1523 (2014).
52. Kalluri, R. The biology and function of fibroblasts in cancer. *Nat. Rev. Cancer* **16**, 582–598 (2016).
53. Dominguez, C. X. et al. Single-cell RNA sequencing reveals stromal evolution into LRRC15⁺ myofibroblasts as a determinant of patient response to cancer immunotherapy. *Cancer Discov.* **10**, 232–253 (2020).
54. Kieffer, Y. et al. Single-cell analysis reveals fibroblast clusters linked to immunotherapy resistance in cancer. *Cancer Discov.* **10**, 1330–1351 (2020).
55. Chauhan, V. P. et al. Reprogramming the microenvironment with tumor-selective angiotensin blockers enhances cancer immunotherapy. *Proc. Natl Acad. Sci. USA* **116**, 10674–10680 (2019).
56. Lu, C. W. et al. WDR5–H3K4me3 epigenetic axis regulates OPN expression to compensate PD-L1 function to promote pancreatic cancer immune escape. *J. Immunother. Cancer* **9**, e002624 (2021).
57. Zhu, Y. et al. Disruption of tumour-associated macrophage trafficking by the osteopontin-induced colony-stimulating factor-1 signalling sensitises hepatocellular carcinoma to anti-PD-L1 blockade. *Gut* **68**, 1653–1666 (2019).
58. Cabrita, R. et al. Tertiary lymphoid structures improve immunotherapy and survival in melanoma. *Nature* **577**, 561–565 (2020).
59. Helmkink, B. A. et al. B cells and tertiary lymphoid structures promote immunotherapy response. *Nature* **577**, 549–555 (2020).
60. Fridman, W. H. et al. B cells and tertiary lymphoid structures as determinants of tumour immune contexture and clinical outcome. *Nat. Rev. Clin. Oncol.* **19**, 441–457 (2022).

Publisher's note Springer Nature remains neutral with regard to jurisdictional claims in published maps and institutional affiliations.

Springer Nature or its licensor (e.g. a society or other partner) holds exclusive rights to this article under a publishing agreement with the author(s) or other rightsholder(s); author self-archiving of the accepted manuscript version of this article is solely governed by the terms of such publishing agreement and applicable law.

© The Author(s), under exclusive licence to Springer Nature America, Inc. 2024

¹Department of Thoracic Surgery, Shanghai Pulmonary Hospital, School of Medicine, Tongji University, Shanghai, China. ²Key Laboratory of Spine and Spinal Cord Injury Repair and Regeneration of Ministry of Education, Department of Orthopedics, Tongji Hospital, School of Life Science and Technology, Tongji University, Shanghai, China. ³Frontier Science Center for Stem Cell Research, School of Life Sciences and Technology, Tongji University, Shanghai, China. ⁴State Key Laboratory of Cell Biology, Center for Excellence in Molecular Cell Science, Shanghai Institute of Biochemistry and Cell Biology, Chinese Academy of Sciences, University of Chinese Academy of Sciences, Shanghai, China. ⁵Department of Pathology, Shanghai Pulmonary Hospital, School of Medicine, Tongji University, Shanghai, China. ⁶Stem Cell Translational Research Center, Tongji Hospital, School of Medicine, Tongji University, Shanghai, China. ⁷Central Laboratory, Shanghai Pulmonary Hospital, School of Medicine, Tongji University, Shanghai, China. ⁸National Key Laboratory of Autonomous Intelligent Unmanned Systems, Tongji University, Shanghai, China. ⁹Frontier Science Center for Intelligent Autonomous Systems, Tongji University, Shanghai, China. ¹⁰Department of Thoracic Surgery, The First Affiliated Hospital of Shihezi University Medical College, Shihezi, China. ¹¹These authors contributed equally: Yilv Yan, Dongqing Sun, Junjie Hu, Yue Chen. ¹²These authors jointly supervised this work: An Zeng, Lele Zhang, Yi Eve Sun, Chenfei Wang, Peng Zhang.  e-mail: azeng@sibcb.ac.cn; zhanglele@tongji.edu.cn; yi.eve.sun@gmail.com; 08chenfeiwang@tongji.edu.cn; zhangpeng1121@tongji.edu.cn

Methods

Patient cohorts and sample collection

We conducted a prospective study in patients with resectable NSCLC lacking *EGFR*/*ALK* mutations who received neoadjuvant ICB-chemotherapy (PD-1 inhibitors plus platinum-based chemotherapy). Before tissue acquisition and genomic sequencing for each patient, we obtained institutional review board approval from the Shanghai Pulmonary Hospital (K21-294) and all patients provided written informed consent. Primary tumor tissues were obtained via percutaneous pulmonary biopsy, bronchoscopy biopsy or endobronchial ultrasound biopsy before drug administration. Patients were treated with two to four cycles of neoadjuvant ICB-chemotherapy followed by surgery. More information is provided in Supplementary Table 1. Fresh tumor tissues were collected immediately following surgical resection.

Spatial transcriptomics data collection pre-treatment

DSP profiling (supported by YuceBio Technology) was performed on primary tumor tissues according to previously published methods⁶¹. Briefly, formalin-fixed, paraffin-embedded sections were hybridized using ultraviolet-photocleavable barcode-conjugated RNA in situ hybridization probes to capture and profile messenger RNA. Tumors and adjacent normal tissues were stained for PanCK, α -SMA and CD20 markers. Slides were then loaded onto the GeoMx instrument for region of interest (ROI) selection based on immunofluorescence images and the results were confirmed by pathologists. Auto-segmentation was performed using custom ultraviolet illumination masks to create ROIs that resulted in photocleavable tags being released specifically in tumors (PanCK⁺ staining and tumor-enriched segments), boundaries (PanCK⁻ and α -SMA⁺ staining and an adjacent tumor region), stromal regions (α -SMA⁻ staining and normal tissue) and lymphoid aggregates (CD20⁺ staining). Cleaved barcodes were collected from each ROI and quantified via sequencing.

The GeoMx NGS Pipeline (version 2.2.0.2) was utilized to convert sequenced FASTQ files into DCC files. The data were subjected to quality control, including technical signal, technical background, probe and normalization. Technical signal quality control was executed to eliminate ROIs in cases where the alignment rate of the reads against the template sequence was <80%. The technical background included three indicators: a no template control (NTC) count; a negative probe count; and ROI parameters. The NTC count was employed to identify and detect template contamination. Any ROIs with an NTC number exceeding 1,000 were eradicated. The overall technical signal level was determined using the negative probe count, with the threshold being set to four counts. Furthermore, the parameters of the ROI were measured by the number of nuclei as well as the surface area. To meet the quality control standards, an ROI had to have a nucleus count of >100. The sizes of ROIs were standardized using cell numbers and area normalization to avoid inconsistencies across them. High-quality data were then normalized with Quantile 3 (ref. 62) and used for downstream analysis. Immune and stromal cell abundances in the TME were determined with deconvolution analysis conducted using scTAPE (version 1.0)⁶³.

Spatial transcriptomics data collection post-treatment

The 10x Genomics Visium spatial transcriptomics platform was used to analyze the transcriptome of cellular components within the tissue context from the immunotherapy-treated NSCLC tumors. Two to three pieces of tumor were embedded in optimal cutting temperature compound by placing them cut side down into a plastic mold. The optimal cutting temperature compound-filled mold was then snap frozen in chilled isopentane and stored at -80 °C until use. Cryosections were then cut at 10 μ m thickness and prepared for subsequent experiments, including H&E staining, permeabilization and library construction. Tissue optimization and library preparation were performed according to the manufacturer's instructions with 10 min of permeabilization.

The barcoded libraries were sequenced using an Illumina NovaSeq 6000 platform with the PE150 sequencing mode. Raw sequencing data of spatial transcriptomics were subjected to quality control and mapped to the reference genome using Space Ranger (version 1.1).

scRNA-seq data generation and quality control

Details on tissue dissociation, the preparation of single-cell suspension and scRNA-seq can be found in Supplementary Note 4. For the BD Rhapsody platform, raw FASTQ files were processed using the BD Rhapsody Whole Transcriptome Analysis pipeline (https://www.bdbiosciences.com/content/dam/bdb/marketing-documents/BD_Single_Cell_Genomics_Bioinformatics_Handbook.pdf) to obtain a unique molecular identifier (UMI) matrix for each sample. For the Singleron platform, raw reads were processed to generate gene expression matrices with the CeleScope pipeline (<https://github.com/singleron-RD/CeleScope>). The matrix of read counts per sample was further analyzed with the Seurat⁶⁴ package (version 4.0.4) in the R software (version 4.1.1). For each cell, we used four quality control measures. Cells falling into any of the following four categories were excluded: (1) <400 expressed genes; (2) >25% UMIs of mitochondrial genes; (3) >25% UMIs of ribosomal genes; and (4) a housekeeping score (defined as the sum of the UMIs of three canonical housekeeping genes: *ACTB*, *GAPDH* and *MALAT1*) of <1. To exclude data from droplets containing more than one cell, doublet detection and removal were performed using Scrublet⁶⁵. An expected doublet rate parameter of 0.025 was used and doublet score thresholds were chosen manually to divide putative singlet and neotypic doublet modes in the score distribution. Predicted doublets were then removed from gene-by-barcode matrices.

scRNA-seq data processing, cross-platform integration and clustering

The gene expression matrices were normalized using the NormalizeData function with default parameters. The normalized data were then scaled using the ScaleData function, with the unwanted variation regressed out from total counts by setting vars.to.regress=c("nCount_RNA"). The top 3,000 highly variable genes were detected using the FindVariableFeatures function. Principal component analysis (PCA) was performed based on the 3,000 most variable features using the RunPCA function. We observed a strong batch effect between the BD Rhapsody and Singleron platforms from the PCA plot. To adjust technical sources of variation between platforms, we used Harmony⁶⁶ (version 0.1.0). The first 20 principal components and a resolution of 0.6 were used with the FindNeighbors and FindClusters functions. Dimension reduction was performed using the RunUMAP function. Major cell lineages were assigned to each cluster of cells using the abundance of canonical marker genes: epithelial cells (*EPCAM*), CD31⁻ stromal cells (*JTGB1* (*CD29*)⁺ and *PECAMI* (*CD31*)), endothelial cells (*PECAMI*), T cells (*CD3D* and *CD3E*), B cells (*CD79A* and *MS4A1*), plasma cells (*CD79A* and *MZB1*), monocytes/macrophages (*CD14* and *CD68*), dendritic cells (*HLA-DRA* and *CD1C*), neutrophils (*FCGR3B*) and mast cells (*MS4A2* and *KIT*).

Cell subpopulation identification

Cycling immune cells were picked out for reclustering to separate T cells, B cells, plasma cells and monocytes/macrophages. Each of the major lineages was then extracted to perform the second clustering, as described above, to identify subpopulations. We further clustered epithelial cells, fibroblasts, T cells, B cells and monocytes/macrophages individually. We used a resolution of 0.4 for epithelial cells, 0.3 for CD31⁻ stromal cells, 0.6 for T cells, 0.3 for B cells and 0.4 for monocytes/macrophages. Notably, after performing sublineage clustering, we manually removed clusters expressing two or more major lineage markers (such as *LYZ* for myeloid cells and *CD3E* for T cells) from the uniform manifold approximation and projection (UMAP) plot, which were possible doublets missed by Scrublet.

CNV estimation and identification of malignant cells

To identify malignant cells among epithelial cells, we used the infercnvpy algorithm (version 0.2.0; <https://github.com/icbi-lab/infercnvpy>) to estimate CNVs. The infercnvpy algorithm was run with stromal cells (CD31⁻ stromal cells and endothelial cells) as a normal reference and with default parameters. The CNV scores for each cell were calculated using the infercnvpy.tl.cnv_score function.

Cellular fraction calculation

For each sample, we calculated the cellular fraction for each major immune lineage (T cells, B cells, myeloid cells and so on). For the sub-populations of major cell lineages, cellular proportions were calculated using the fractions in corresponding major lineages. The samples that had fewer than ten cells in a major lineage were removed for downstream statistical analysis. All of the statistical tests used are noted in the figure captions.

Gene module enrichment analysis

To estimate the signatures of the CAF phenotypes iCAF and myCAF, we calculated the enrichment scores for fibroblasts using the AddModuleScore function in Seurat, with the gene list reported by Öhlund et al.²⁴. The enrichment of hallmark signatures and metabolic activity within each fibroblast subset was quantified using the AUCell algorithm⁶⁷ (version 1.8.0) with Hallmark and Kyoto Encyclopedia of Genes and Genomes pathways. To quantify the tumor cell state, we defined cell states using a set of the 50 most differentially expressed genes for each malignant subset. The scores of tumor cell state were calculated using the R package GSVA (version 1.52.3)⁶⁸.

Ligand–receptor interaction analysis

CellChat (version 1.1.3)⁶⁹ was utilized to infer ligand–receptor interactions. The cell–cell communication network was visualized using the netVisual_aggregate function. After annotating the object with relevant labels and identifying overexpressed genes, the communication probability was inferred using the computeCommunProb function. Cell–cell communications for each cell signaling pathway were generated with the computeCommunProbPathway function. Graphs were generated using the netVisual_chord_gene and netVisual_bubble functions. Receptor–ligand pairs related to DDR1 and summarized using SingleCellSignalR⁷⁰ (<https://github.com/SCA-IRCM/SingleCellSignalR>) were manually added to the default reference.

NicheNet analysis

NicheNet²⁶ (version 1.0.0)—a powerful tool that predicts the ligands driving transcriptomic changes of target cells—was used to identify potential ligands that drive the specific phenotypes of fibroblast subsets. As described previously⁷¹, we used all of the expressed genes of COL11A1⁺ CAFs as the background of genes and the top 50 genes ordered by $\log_2[\text{fold change}]$ as the gene set of interest. Genes were considered to be expressed when they had non-zero values in at least 10% of the cells within a cell type. We only used the expressed receptors in COL11A1⁺ CAFs to construct ligand–receptor interactions and calculate ligand activity using the predict_ligand_activities function.

Survival analysis using the TCGA-LUAD cohort

The fragments per kilobase of transcript per million mapped reads matrix and clinical information on lung adenocarcinoma from the TCGA database were downloaded from UCSC Xena (<http://xena.ucsc.edu/>). The average expression levels of marker genes of a cell type were calculated as the signature of that particular cell type. The patients were divided into high- and low-signature groups using a cutoff value estimated with the survminer (version 0.4.9) R package for COL11A1⁺ CAF signature (Supplementary Table 2). For the signature of SPP1⁺ macrophages, a median value was used to dichotomize patients. The Kaplan–Meier curve was generated using the survival (version 3.2.11)

R package and compared using a log-rank test. A *P* value of <0.05 was considered statistically significant.

Fibroblast subset deconvolution in bulk RNA-seq

To assess whether the abundance of COL11A1⁺ CAFs in NSCLC could be a predictor of immunotherapy responses, we used the CIBERSORTx algorithm⁷² to estimate the fractions of CD31⁻ stromal subsets from bulk RNA-seq data. We first used the UMI matrix of CD31⁻ stromal cells labeled by subset name to create the signature matrix on the CIBERSORTx website (<https://cibersortx.stanford.edu/>) with the setting Min. Expression = 0.4. Then, the raw count matrix of bulk RNA-seq data was used as input to impute cell fractions with the generated signature matrix and default parameters.

Spatial deconvolution using STRIDE

To understand the spatial cell type distribution in the TME, we performed deconvolution on the 10x Visium spatial transcriptomics data using STRIDE²³ (version 0.0.1b) (<https://github.com/wanglabtongji/STRIDE>) with scRNA-seq as a reference. Considering the heterogeneity of TMEs in NSCLC subtypes, STRIDE was implemented within lung adenocarcinoma and lung squamous cell carcinoma samples, respectively. We first performed cell type deconvolution at the major lineage level; the top ~100 differentially expressed genes of each cell type were identified with the FindAllMarkers function of Seurat and used as signature genes to run STRIDE. To decipher the spatial distribution of cell subtypes, we also performed deconvolution at the minor lineage level. Specifically, we identified the top ~100 differentially expressed genes of each subtype and utilized them to run STRIDE within each major lineage cell type separately. STRIDE returns the relative abundances of cell subtypes, meaning that the sum of all subtype proportions within each cell type is 1. Then, the absolute proportion of each cell subtype was calculated as the product of the minor lineage proportion and the corresponding major lineage proportion.

Spatial transcriptomic data analysis

The generated gene-by-spot matrices were analyzed with the Seurat package (version 4.0.4) in R. Before downstream analysis, we filtered out spots with fewer than 200 genes detected and removed genes with fewer than ten read counts or expressed in fewer than three spots. Normalization across spots was performed with the SCTransform function.

To explore the cytotoxic signature, we calculated the enrichment scores for each spot using the AddModuleScore function with the canonical cytotoxic markers (*GZMA*, *GZMB*, *GZMK*, *CNLN1*, *IFNG*, *PRF1* and *NKG7*). Spatial features were visualized with the SpatialFeaturePlot function in Seurat. To estimate the signature of collagen formation in spatial transcriptomics, we calculated enrichment scores using the gene lists from the REACTOME_COLLAGEN_FORMATION pathway (msigdb.v7.5.1.symbols.gmt; downloaded from <https://www.gsea-msigdb.org/gsea/index.jsp>).

To explore the cell type contexts, we performed PCA and then tSNE using the RunPCA and RunUMAP functions based on the cell type proportion inferred by STRIDE. A total of 15 cell contexts were defined by the FindNeighbors and FindClusters functions with the parameters dims=1:10 and Resolution=0.8, respectively.

Visualization of cell abundance and gene expression in Visium data

As previously reported⁷³, although multiple subpopulations from the same cell lineage could theoretically be present in a given spatially barcoded spot, for the sake of stringency (given the low number of cells per spot), we assumed that the most abundant subpopulation inferred per cell type had the dominant effect. Therefore, we displayed the spatial distribution of COL11A1⁺ CAFs in the COL11A1⁺ CAF-dominant spots and the distribution of ADH1B⁺ CAFs in ADH1B⁺ CAF-dominant spots. For SPP1⁺ and CXCL9⁺ macrophages, their

colocalization and communication with COL1A1⁺ CAFs had important biological effects, so we displayed the spatial distributions of SPP1⁺ and CXCL9⁺ macrophages in SPP1⁺ macrophage-dominant or CXCL9⁺ macrophage-dominant spots.

Since *CD44* was widely expressed in immune, stromal and epithelial cells, we normalized the expression of *CD44* in spatial transcriptomics by multiplying the fraction of COL1A1⁺ CAFs in a spot to represent the expression of *CD44* in COL1A1⁺ CAFs (Fig. 5c). Besides SPP1⁺ macrophages, malignant cells also expressed *SPP1*. Therefore, we manually adjusted the expression of *SPP1* in tumor spots to 0 to display the expression of *SPP1* in non-tumor regions and perform SPP1–CD44 colocalization analysis between SPP1⁺ macrophages and COL1A1⁺ CAFs in the Visium data (Fig. 5c).

Colocalization analysis in Visium data

We used an arithmetic product strategy to estimate the colocalization level at the spot level in spatial transcriptomics. For each spot, the colocalization level of a gene A–gene B pair was determined by the expression both within the spot and with surrounding spots. To be specific, for a spot (X), the arithmetic product of the expression level of gene A ($X_{\text{gene A}}$) and gene B ($X_{\text{gene B}}$) was defined as the colocalization level within the spot, and the weight was set as 1. For the colocalization level from its surrounding spots (Y_i), the weight was set to 0.5. Here we only considered the colocalization level between a spot and the nearest spots ($n \leq 6$). Then, the colocalization level of the gene A–gene B pair in spot X was calculated as

$$\text{Gene A – gene B colocalization level} = X_L X_R + 0.5 \sum_{i=1}^n Y_{i,\text{gene A}} Y_{i,\text{gene B}}$$

TLS identification based on H&E image and Visium data

To study TLSs systematically, we developed an approach to identify all TLSs in spatial transcriptomics slides (<https://github.com/wanglabtongji/Scanner>), which combined both H&E staining images and spatial transcriptomics data (Extended Data Fig. 6f). TLSs primarily comprise lymphocytes with little cytoplasm and are organized compactly, resulting in darker purple loci separated from the surrounding brighter pink stroma. H&E images were converted to grayscale, and darker loci were extracted as potential TLSs. We checked the deconvolved cell type composition of spots within the extracted region, and the darker loci with a high percentage of lymphocytes (B and T cells) (>15%) were considered as TLSs. Of note, only TLSs with more than two spots were considered in downstream analysis. The scikit-image toolbox was applied for image processing.

Integrative analysis of TLSs

Each identified TLS covered multiple spots. The averaged gene expression of each spot was used to represent the gene expression profile of each TLS. To enable comprehensive and unbiased analyses, we integrated TLSs from all samples together. First, we performed PCA of TLSs in each sample separately. TLSs in P06 samples exhibited greater diversity among all samples. Given this, we utilized TLSs from P06 as a reference and projected TLSs from other samples onto the P06 space. Based on the top 100 genes with high positive or negative contributions from PC1 and PC2, the pseudotime of each TLS was calculated using the Monocle 2 (ref. 74) *orderCells* function. To classify TLSs into different stages, we performed *k*-means clustering on TLSs using the first two principal components (that is, PC1 and PC2) with *k* set to 4. The four clusters were then defined as lymphoid aggregates, activated TLSs, declining TLSs and late TLSs by their expression of TLS-related genes, including LTi markers (*RORC* and *IL7R*)⁷⁵ and functional cytokines (*LTB* and *CXCL13*)¹². The cluster with a high LTi signature represented the early initiation stage and the cluster with high expression of cytokines represented the activated TLS state. The cluster with decreasing cytokine expression and the one with low cytokine expression were

defined as declining and late TLSs, respectively. The process from the early to the activated state was defined as activation and the process after activation from the declining stage to the late state was defined as recession (Fig. 6c).

Differential expression analysis in TLSs

To identify the differences between late TLSs for samples with different responses, we compared the expression of all genes in spots of late TLSs from the NMPR versus pCR group. The significance of each gene was defined by Wilcoxon rank-sum test and adjusted by Bonferroni correction. Significantly highly expressed genes in the NMPR group (adjusted *P* value < 5×10^{-3} and average log[fold change] > 0.25) were selected for pathway enrichment analysis. The hypoxia signature was defined as the intersection between the significantly highly expressed genes in the NMPR group and genes from the HALLMARK_HYPOXIA gene set (Supplementary Table 3). The activated TLS signature was defined as the highly expressed genes in activated TLS spots compared with lymphoid aggregate spots (Supplementary Table 4).

Statistics and reproducibility

In Figs. 4a,l and 6g, a two-sided Wilcoxon test was used to determine statistical significance. In Fig. 4k,j, a one-sided Wilcoxon test was used to determine statistical significance. In Figs. 4f,h and 5a, two-sided *P* values were calculated by Pearson's correlation test. The other statistical methods used are described in the captions. All immunofluorescence results were replicated independently at least three times to ensure reproducibility. A *P* value of <0.05 was used as the threshold for significance, except where indicated otherwise. No statistical method was used to predetermine the sample size.

Reporting summary

Further information on research design is available in the Nature Portfolio Reporting Summary linked to this article.

Data availability

Raw scRNA-seq and spatial transcriptomics data have been deposited to the Genome Sequence Archive of the BIG Data Center at the Beijing Institute of Genomics, Chinese Academy of Science, under accession number HRA002509 (accessible at <http://bigd.big.ac.cn/gsa-human>). Processed bulk RNA-seq, scRNA-seq and spatial transcriptomics data are available from Zenodo (accessible at <https://zenodo.org/records/8227624>)⁷⁶. The bulk RNA-seq data of the independent NSCLC cohort⁶ were acquired from the Gene Expression Omnibus (<https://www.ncbi.nlm.nih.gov/geo>) with the accession GSE207422. The bulk RNA-seq data of the Stand Up To Cancer–Mark Foundation for Cancer Research cohort³¹ are available from Zenodo (accessible at <https://zenodo.org/records/7849582>)⁷⁷. The bulk RNA-seq data of the OAK and POPLAR cohorts³⁰ were acquired from the European Genome-Phenome Archive (<https://ega-archive.org>) with the accession EGAS00001005013. The bulk RNA-seq data of the melanoma cohort³² were acquired from the Gene Expression Omnibus with the accession GSE78220.

Code availability

The code for identifying the TLSs in spatial transcriptomics slides can be found at <https://github.com/wanglabtongji/Scanner>. Code for inferring the cell type distribution in spatial transcriptomics data can be found at <https://github.com/wanglabtongji/STRIDE>.

References

61. Merritt, C. R. et al. Multiplex digital spatial profiling of proteins and RNA in fixed tissue. *Nat. Biotechnol.* **38**, 586–599 (2020).
62. Zhao, Y., Wong, L. & Goh, W. W. B. How to do quantile normalization correctly for gene expression data analyses. *Sci. Rep.* **10**, 15534 (2020).

63. Chen, Y. et al. Deep autoencoder for interpretable tissue-adaptive deconvolution and cell-type-specific gene analysis. *Nat. Commun.* **13**, 6735 (2022).
64. Hao, Y. H. et al. Integrated analysis of multimodal single-cell data. *Cell* **184**, 3573–3587.e29 (2021).
65. Wolock, S. L., Lopez, R. & Klein, A. M. Scrublet: computational identification of cell doublets in single-cell transcriptomic data. *Cell Syst.* **8**, 281–291.e9 (2019).
66. Korsunsky, I. et al. Fast, sensitive and accurate integration of single-cell data with Harmony. *Nat. Methods* **16**, 1289–1296 (2019).
67. Aibar, S. et al. SCENIC: single-cell regulatory network inference and clustering. *Nat. Methods* **14**, 1083–1086 (2017).
68. Haenzelmann, S., Castelo, R. & Guinney, J. GSVA: gene set variation analysis for microarray and RNA-seq data. *BMC Bioinformatics* **14**, 7 (2013).
69. Jin, S. et al. Inference and analysis of cell-cell communication using CellChat. *Nat. Commun.* **12**, 1088 (2021).
70. Cabello-Aguilar, S. et al. SingleCellSignalR: inference of intercellular networks from single-cell transcriptomics. *Nucleic Acids Res.* **48**, e55 (2020).
71. Cheng, S. J. et al. A pan-cancer single-cell transcriptional atlas of tumor infiltrating myeloid cells. *Cell* **184**, 792–809.e23 (2021).
72. Newman, A. M. et al. Determining cell type abundance and expression from bulk tissues with digital cytometry. *Nat. Biotechnol.* **37**, 773–782 (2019).
73. Luca, B. A. et al. Atlas of clinically distinct cell states and ecosystems across human solid tumors. *Cell* **184**, 5482–5496.e28 (2021).
74. Qiu, X. J. et al. Reversed graph embedding resolves complex single-cell trajectories. *Nat. Methods* **14**, 979–982 (2017).
75. Germain, C., Gnjatic, S. & Dieu-Nosjean, M. C. Tertiary lymphoid structure-associated B cells are key players in anti-tumor immunity. *Front. Immunol.* **6**, 67 (2015).
76. Yan, Y. Multi-omic profiling highlights factors associated with resistance to immuno-chemotherapy in non-small cell lung cancer. Zenodo <https://doi.org/10.5281/zenodo.13901289> (2024).
77. Holton, M., Arniella, M., Ravi, A. & Getz, G. Genomic and transcriptomic analysis of checkpoint blockade response in advanced non-small cell lung cancer. Zenodo <https://doi.org/10.5281/zenodo.7849582> (2023).

Acknowledgements

This work was supported by the National Natural Science Foundation of China (82125001 (P.Z.), 62088101 (C.W.), 82201948 (L.Z.), 32170660 (C.W.) and 82030035 (Y.E.S.)), National Key R&D Program of China (grant 2022YFA1106000 (C.W.)), Clinical Research Plan of Shanghai Hospital Development Center (grant SHDC2020CR2020B (P.Z.)), Innovation Program of the Shanghai Municipal Education Commission (grant 2023ZKZD33 (P.Z.)), Shanghai Pulmonary Hospital (FKCX1904 (P.Z.), FKQYQ2308 (L.Z.) and FKLY20004 (P.Z.)), Shanghai Pilot Program for Basic Research (C.W.), Shanghai Municipal Science and Technology Major Project (2021SHZDZX0100 (C.W.)), Peak Disciplines (Type IV) of Institutions of Higher Learning in Shanghai (C.W. and Y.E.S.) and Fundamental Research Funds for the Central Universities (22120240435 (C.W.)).

Author contributions

P.Z., C.W., Y.E.S., L.Z. and A.Z. conceived of and designed the study. H.Y., Y.X., Z.H., H.X., X.Z., D.B., F.S., Y.C., L.H., C.W., A.Z. and L.Z. developed and performed the experiments or collected data. Y.Y., D.S., J.H., L.S. and C.W. designed and performed the computation and statistical analyses. Y.Y., D.S., J.H., O.R.F., H.H., L.Z., Y.E.S., C.W. and P.Z. wrote, reviewed and edited the manuscript.

Competing interests

The authors declare no competing interests.

Additional information

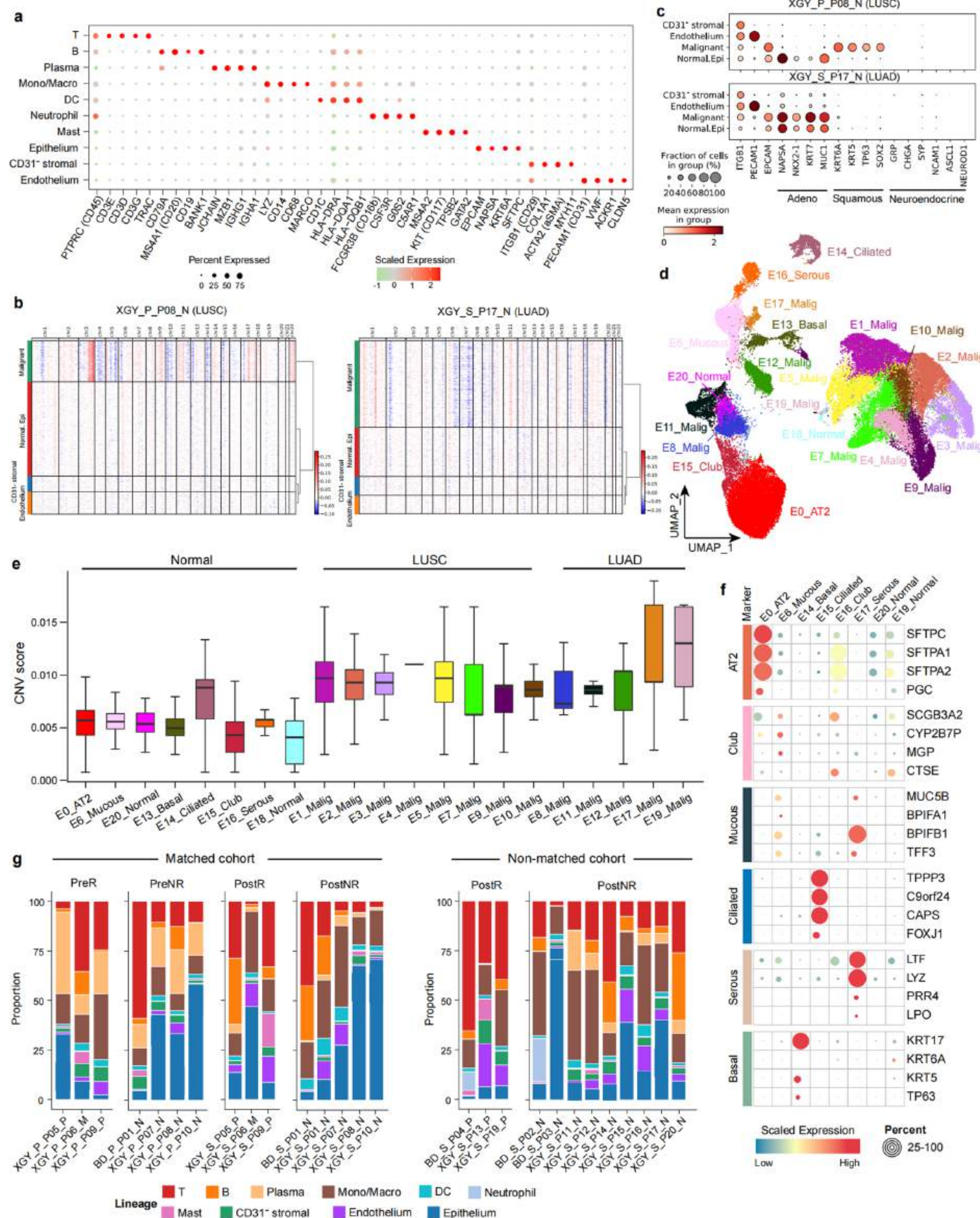
Extended data is available for this paper at <https://doi.org/10.1038/s41588-024-01998-y>.

Supplementary information The online version contains supplementary material available at <https://doi.org/10.1038/s41588-024-01998-y>.

Correspondence and requests for materials should be addressed to An Zeng, Lele Zhang, Yi Eve Sun, Chenfei Wang or Peng Zhang.

Peer review information *Nature Genetics* thanks Sydney Shaffer and the other, anonymous, reviewer(s) for their contribution to the peer review of this work.

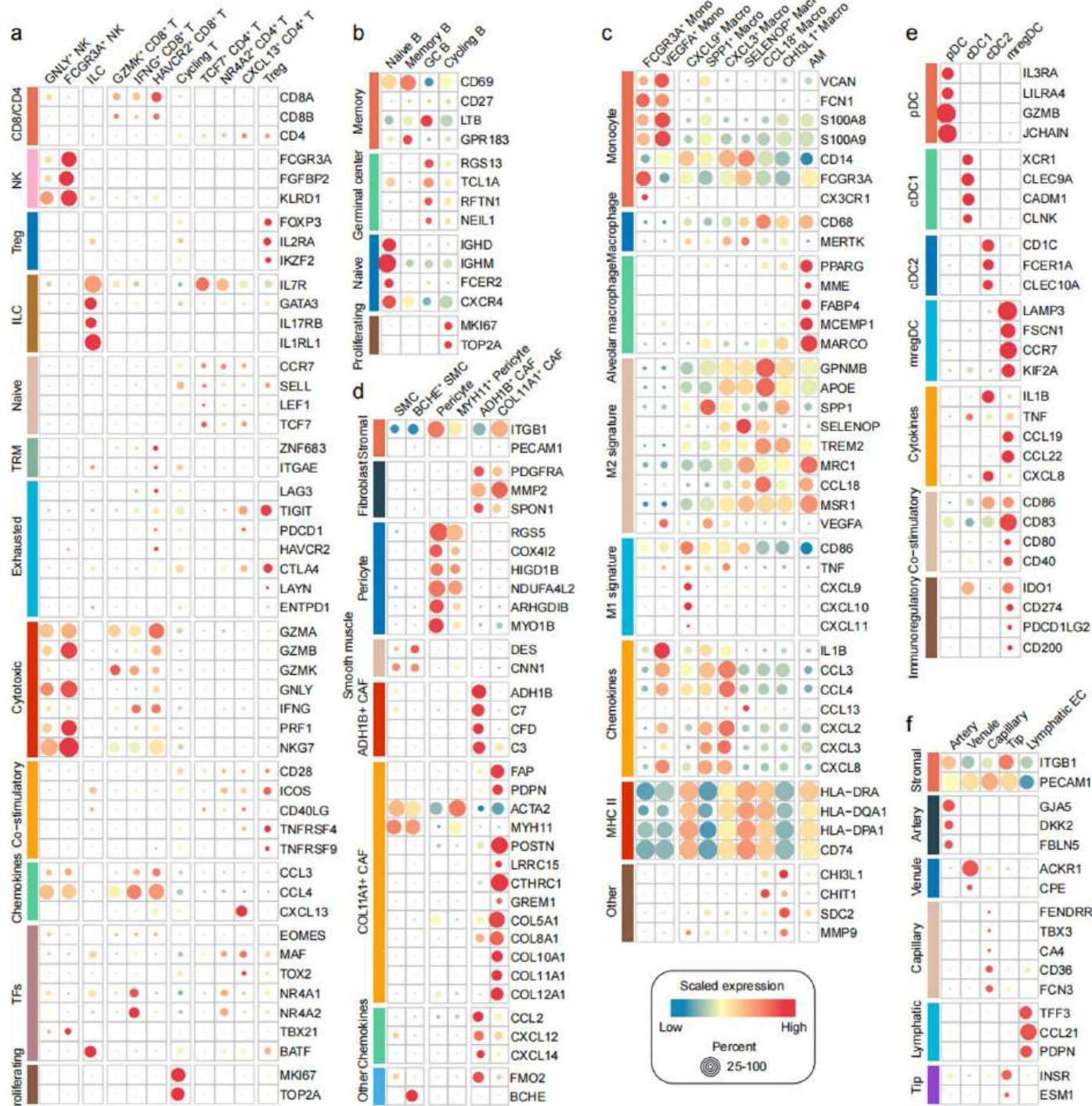
Reprints and permissions information is available at www.nature.com/reprints.



Extended Data Fig. 1 | See next page for caption.

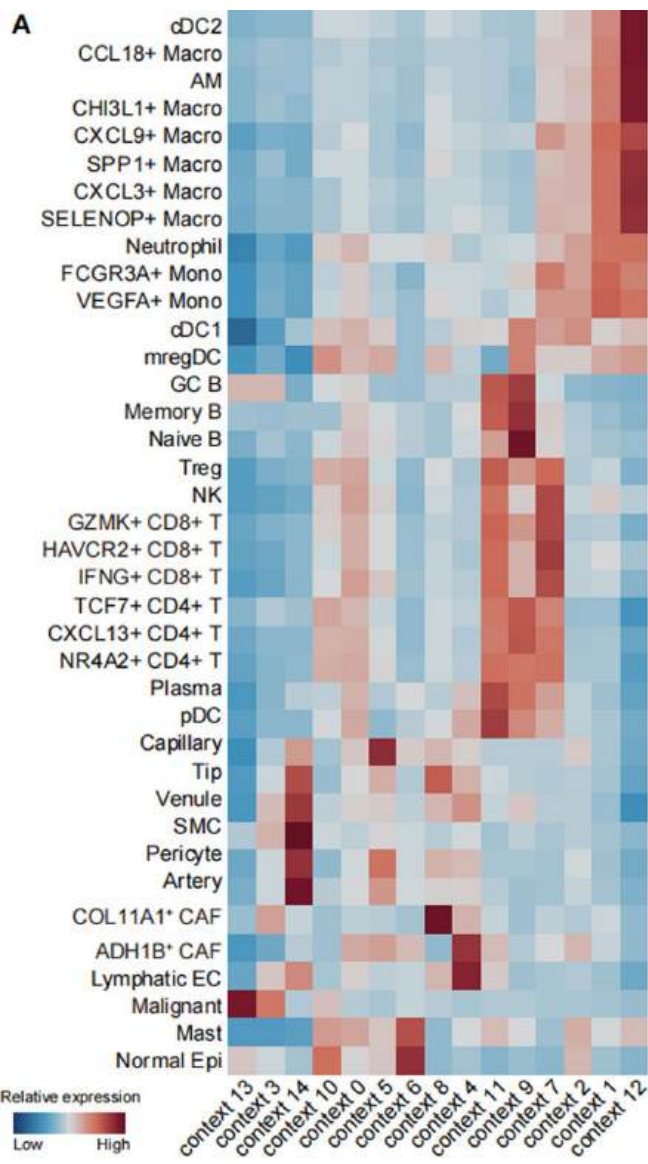
Extended Data Fig. 1 | Characterization of immunotherapy-treated NSCLC by combined scRNA-seq and spatial transcriptomic analysis. **a**, Dot-heat plot showing marker genes for each major lineage. The color gradient represents the expression level, and the diameter represents the percentage of cells. **b**, Examples of inferred CNV profiles of malignant cells and normal epithelial cells, with endothelium and CD31⁺ stromal cells as references. Left panel: lung squamous cell carcinoma (LUSC). Right panel: lung adenocarcinoma (LUAD). **c**, Dot-heat plot showing the markers of adeno, squamous and

neuroendocrine tumors in P08 and P17. **d**, UMAP plot of all epithelial cells colored by subpopulations. **e**, Boxplot showing the CNV score of each epithelium subpopulation. Box limits denote the first and third quartiles with the median shown in the center and whiskers covering data within 1.5 \times the interquartile range from the box. **f**, Dot-heat plot showing the marker genes for each normal epithelial cluster. The color gradient represents the scaled expression level, and the diameter represents the percentage of cells. **g**, Bar plot showing the percentage of major lineages for each sample. Related to Fig. 1.

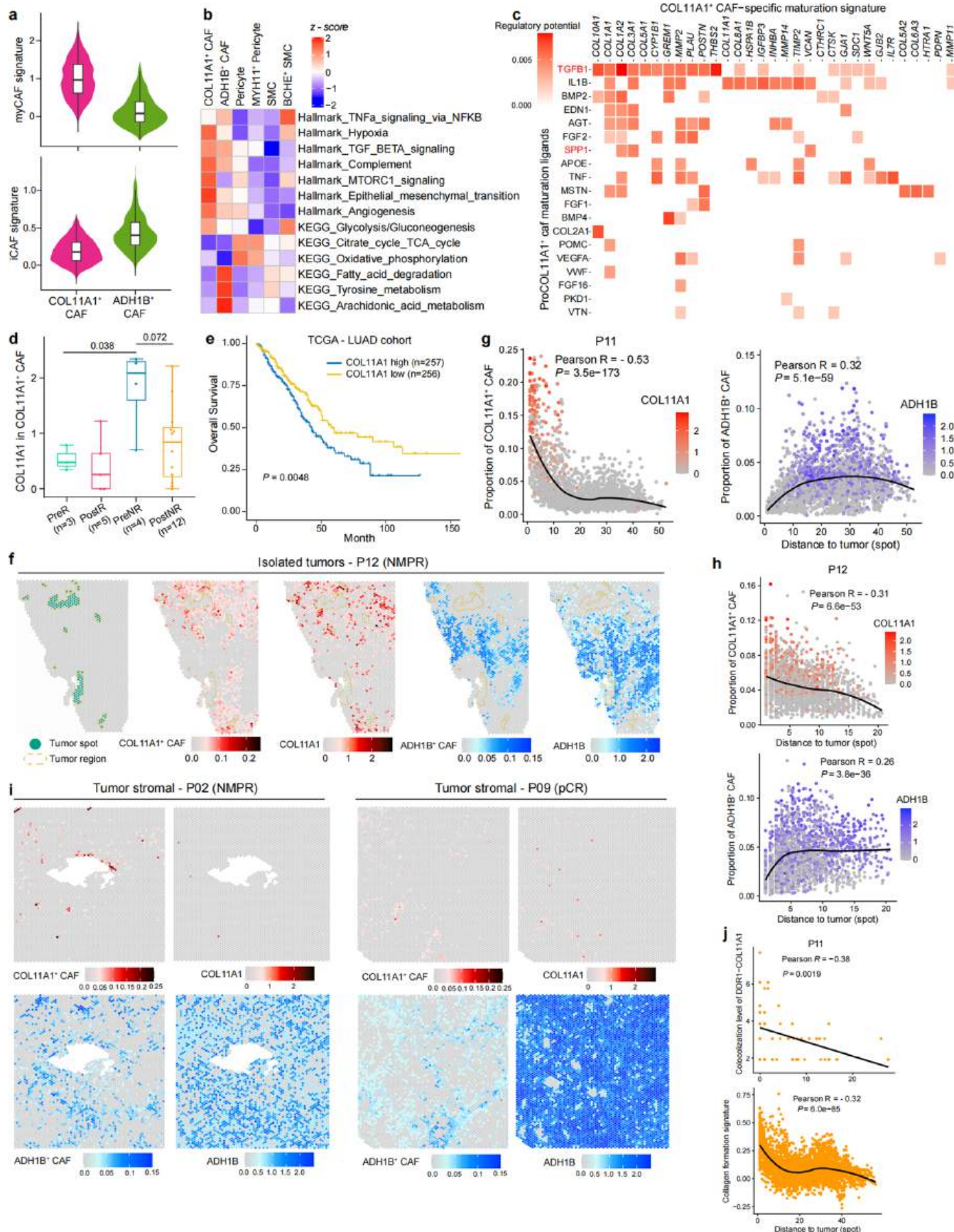


Extended Data Fig. 2 | Characterization of immunotherapy-treated NSCLC by combined scRNA-seq and spatial transcriptomic analysis. **a**, Dot-heat plot showing the marker genes for each T cluster. The color gradient represents the scaled expression level, and the diameter represents the percentage of cells. **b**, Dot-heat plot showing the marker genes for each B cluster. The color gradient represents the scaled expression level, and the diameter represents the percentage of cells. **c**, Dot-heat plot showing the marker genes for each Mono/Macro cluster. The color gradient represents the scaled expression level, and the diameter represents the percentage of cells. **d**, Dot-heat plot showing the marker genes for each CD31⁺ stromal cluster. The color gradient represents the scaled expression level, and the diameter represents the percentage of cells. **e**, Dot-heat plot showing the marker genes for each DC cluster. The color gradient represents the scaled expression level, and the diameter represents the percentage of cells. **f**, Dot-heat plot showing the marker genes for each endothelial cluster. The color gradient represents the scaled expression level, and the diameter represents the percentage of cells. Related to Fig. 1.

diameter represents the percentage of cells. **d**, Dot-heat plot showing the marker genes for each CD31⁺ stromal cluster. The color gradient represents the scaled expression level, and the diameter represents the percentage of cells. **e**, Dot-heat plot showing the marker genes for each DC cluster. The color gradient represents the scaled expression level, and the diameter represents the percentage of cells. **f**, Dot-heat plot showing the marker genes for each endothelial cluster. The color gradient represents the scaled expression level, and the diameter represents the percentage of cells. Related to Fig. 1.



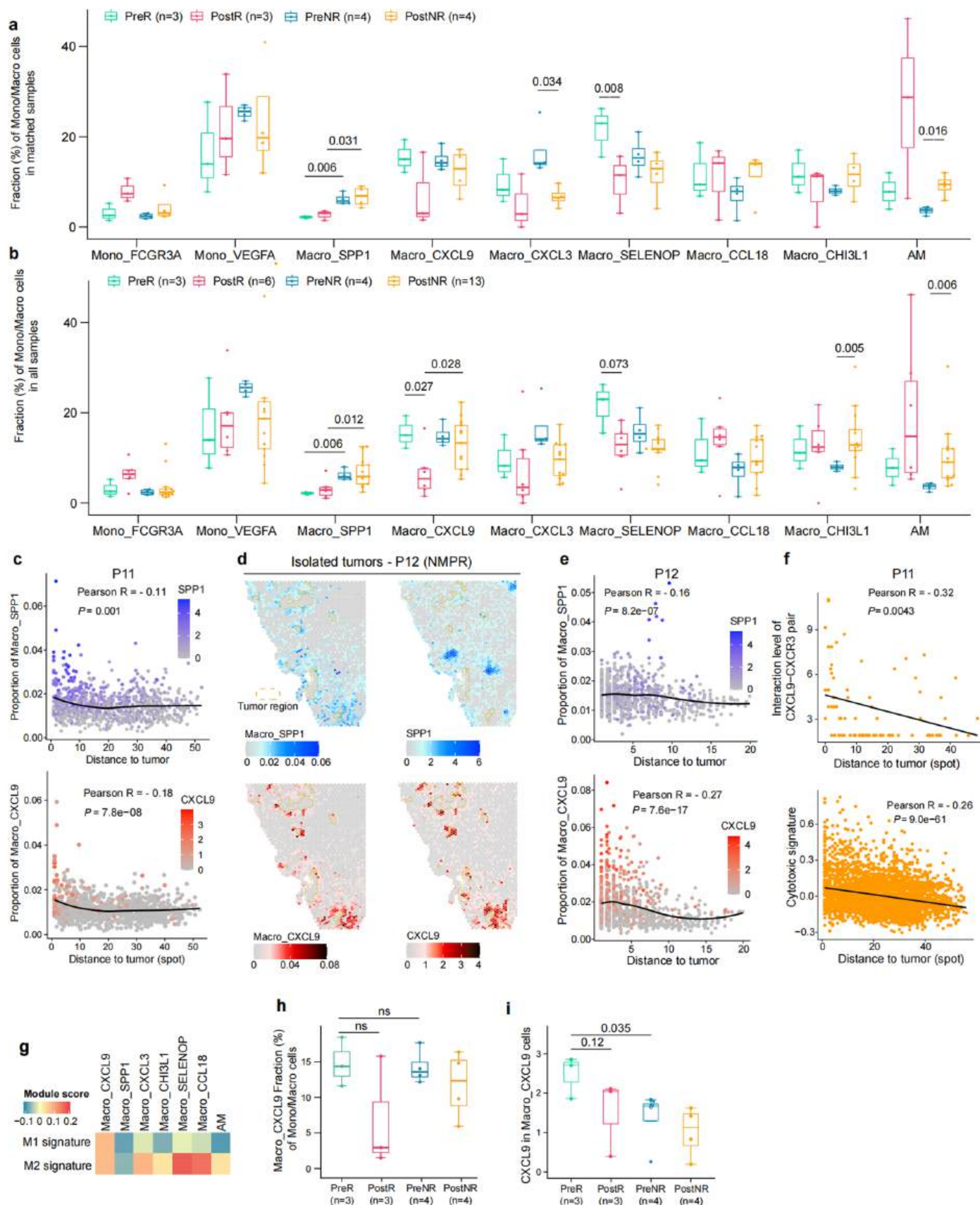
Extended Data Fig. 3 | Spatial mapping of the cellular context in NSCLC after ICB-chemotherapy. **a**, Scaled average cell-type compositions within each cell-type context. Related to Fig. 3.



Extended Data Fig. 4 | See next page for caption.

Extended Data Fig. 4 | Single-cell and spatial transcriptomic analyses of fibroblast subsets after ICB-chemotherapy. **a**, Violin plots showing iCAF and myCAF signature scores in COL11A1⁺ CAFs ($n = 2359$) and ADH1B⁺ CAFs ($n = 956$). Box limits denote the first and third quartiles with the median shown in the center and whiskers covering data within $1.5 \times$ the interquartile range from the box. **b**, Heatmap showing differentially enriched Hallmark and KEGG metabolic pathways in CD31⁻ stromal subsets. **c**, Heatmap showing potential ligands driving the phenotype of COL11A1⁺ CAF cells. **d**, Boxplots showing the average expression of COL11A1 in COL11A1⁺ CAF cells from pre-treatment responders (PreR, $n = 3$), pre-treatment non-responders (PreNR, $n = 4$), post-treatment responders (PostR, $n = 5$) and post-treatment non-responders (PostNR, $n = 12$). The center line indicates the median, and the lower and upper hinges represent the 25th and 75th percentiles. Whiskers denote $1.5 \times$ interquartile range. A two-sided t test was used to determine the statistical significance. **e**, Kaplan-Meier survival curve of the TCGA-LUAD cohort dichotomized by the expression of COL11A1. The survival curves were compared by log-rank test. **f**, Spatial distribution of tumor

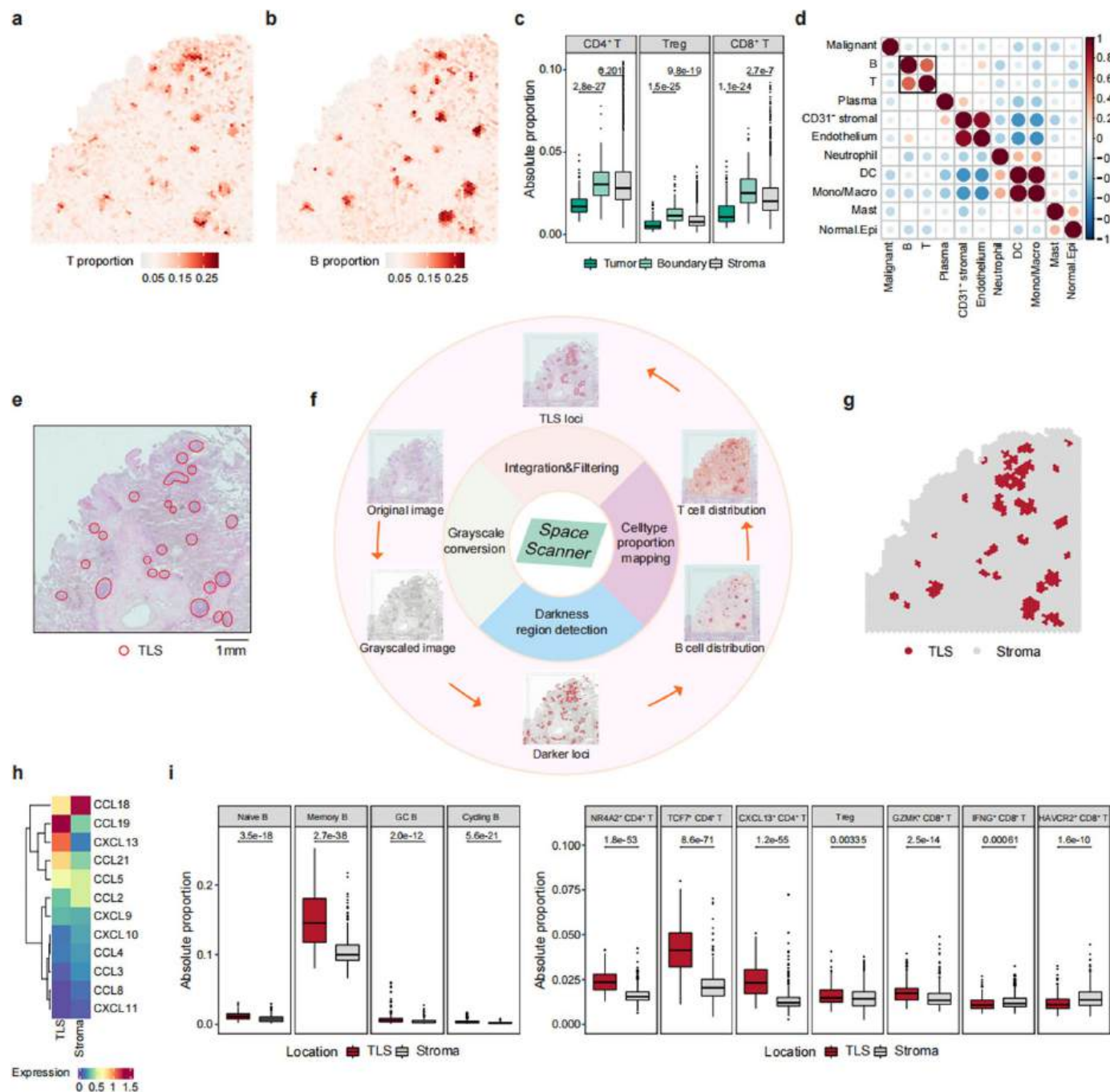
spots, the fractions of COL11A1⁺ CAFs and ADH1B⁺ CAFs and the expression of COL11A1 and ADH1B in the slide of isolated tumor from P12. **g,h**, Scatter plots showing a significantly negative correlation between COL11A1⁺ CAF abundance and distance to tumors (spot) and a positive correlation between ADH1B⁺ CAF abundance and distance to tumors (spot) in the slides of isolated tumor from P11 (g) and P12 (h). The expression levels of COL11A1 or ADH1B in each spot are shown by the color gradient. The curves were fitted using a locally weighted regression (loess) model. The two-sided P values were determined by Pearson's correlation test. **i**, Spatial distribution of tumor spots, fractions of COL11A1⁺ CAFs and ADH1B⁺ CAFs and the expression of COL11A1 and ADH1B in the slides of tumor stromal regions from P02 and P09. **j**, Scatter plot showing a significant negative correlation between the colocalization levels of COL11A1-DDR1 and the collagen formation signatures and distance to tumors (spot) in the slide from P11. The curves were fitted using linear and locally weighted regression (loess) models, respectively. The two-sided P values were determined by Pearson's correlation test. Related to Fig. 4.



Extended Data Fig. 5 | See next page for caption.

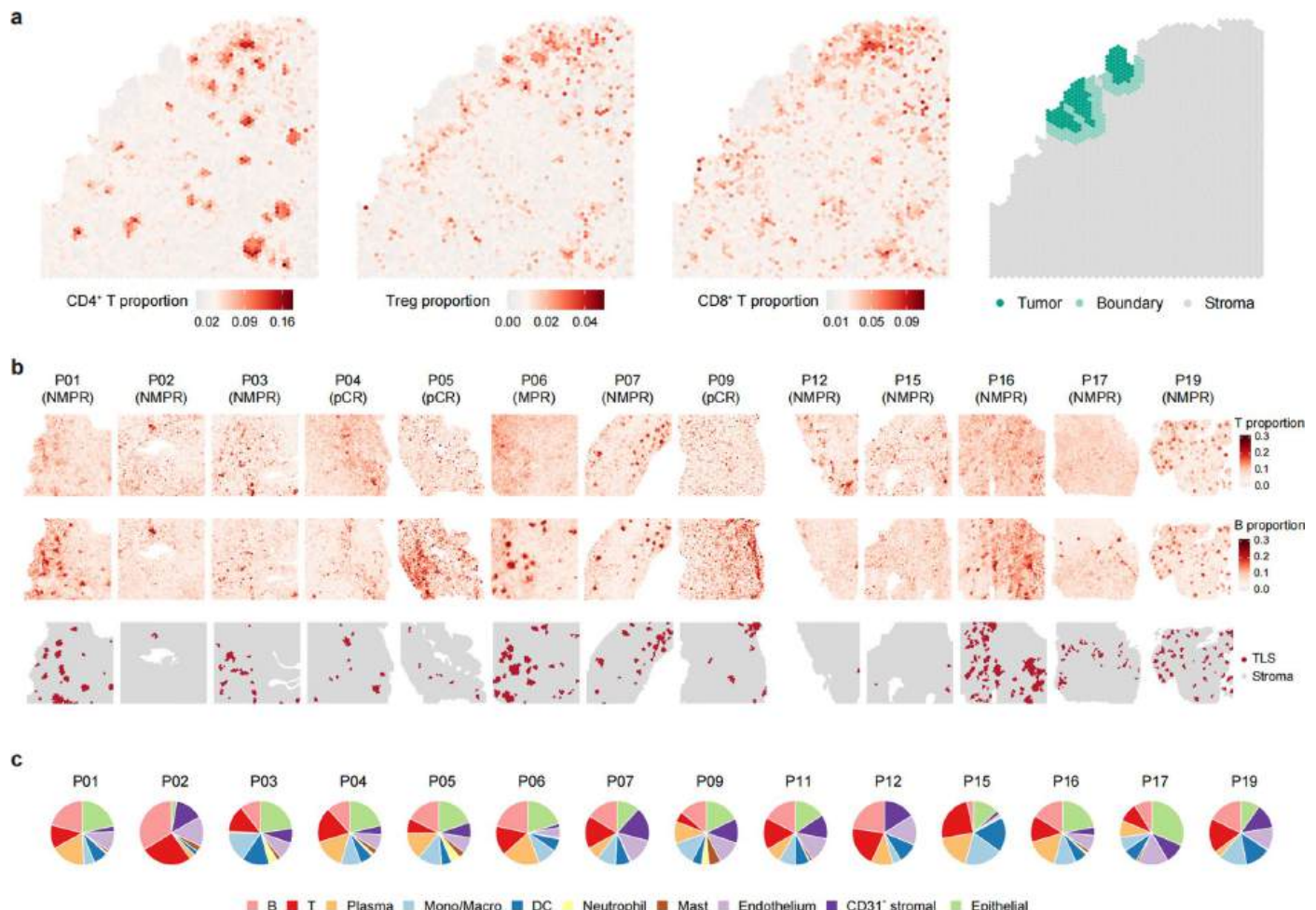
Extended Data Fig. 5 | Spatial transcriptomic and scRNA-seq analyses of macrophage subsets after ICB-chemotherapy. **a**, Boxplots showing the fractions of Mono/Macro subsets in matched samples from 3 responders and 4 non-responders at baseline and post-treatment phase. **b**, Boxplots showing the fractions of Mono/Macro subsets from pre-treatment responders (PreR, n = 3), pre-treatment non-responders (PreNR, n = 4), post-treatment responders (PostR, n = 6) and post-treatment non-responders (PostNR, n = 13). **c**, Scattered plot showing a significant negative correlation between the fraction of SPP1⁺ macrophages or CXCL9⁺ macrophages and distance to tumors (spot) in the slide of isolated tumor from P11. The expression level of SPP1 or CXCL9 in each spot is shown by the color gradient. **d**, Spatial distribution of tumor spots, fractions of SPP1⁺ macrophages and CXCL9⁺ macrophages and the expression of SPP1 and CXCL9 in the slide of isolated tumor from P12. **e**, Scattered plot showing a significant negative correlation between the fractions of SPP1⁺ macrophages or CXCL9⁺ macrophages and the distances to tumors (spot) in the slide of isolated tumor from P12. Expression levels of SPP1 or CXCL9 in each spot are shown by

the color gradient. **f**, Scatter plot showing a significant negative correlation between the colocalization levels of CXCL9-CXCR3 and cytotoxic signature and the distances to tumors (spot) in the slide from P11. **g**, Heatmap showing the averaged module scores of M1 and M2 signatures among macrophage subsets. **h**, Boxplots showing the fractions of CXCL9⁺ macrophages in matched samples from 3 responders and 4 non-responders at baseline and post-treatment. **i**, Box plots of average expression of CXCL9 in CXCL9⁺ macrophages in matched samples from 3 responders and 4 non-responders at baseline and post-treatment phase. This result indicates that CXCL9 expression in macrophages before but not post-treatment is high in responders. In panels **c**, **e** and **f**, the curves were fitted using locally weighted regression (loess), linear and loess models, respectively. Two-sided P values were determined by Pearson's correlation test. In panels **a**, **b**, **h** and **i**, a one-sided t-test was used to determine the statistical significance. For the boxplots, box limits denote the first and third quartiles, with the median shown in the center and whiskers covering data within 1.5× the interquartile range from the box. Related to Fig. 5.



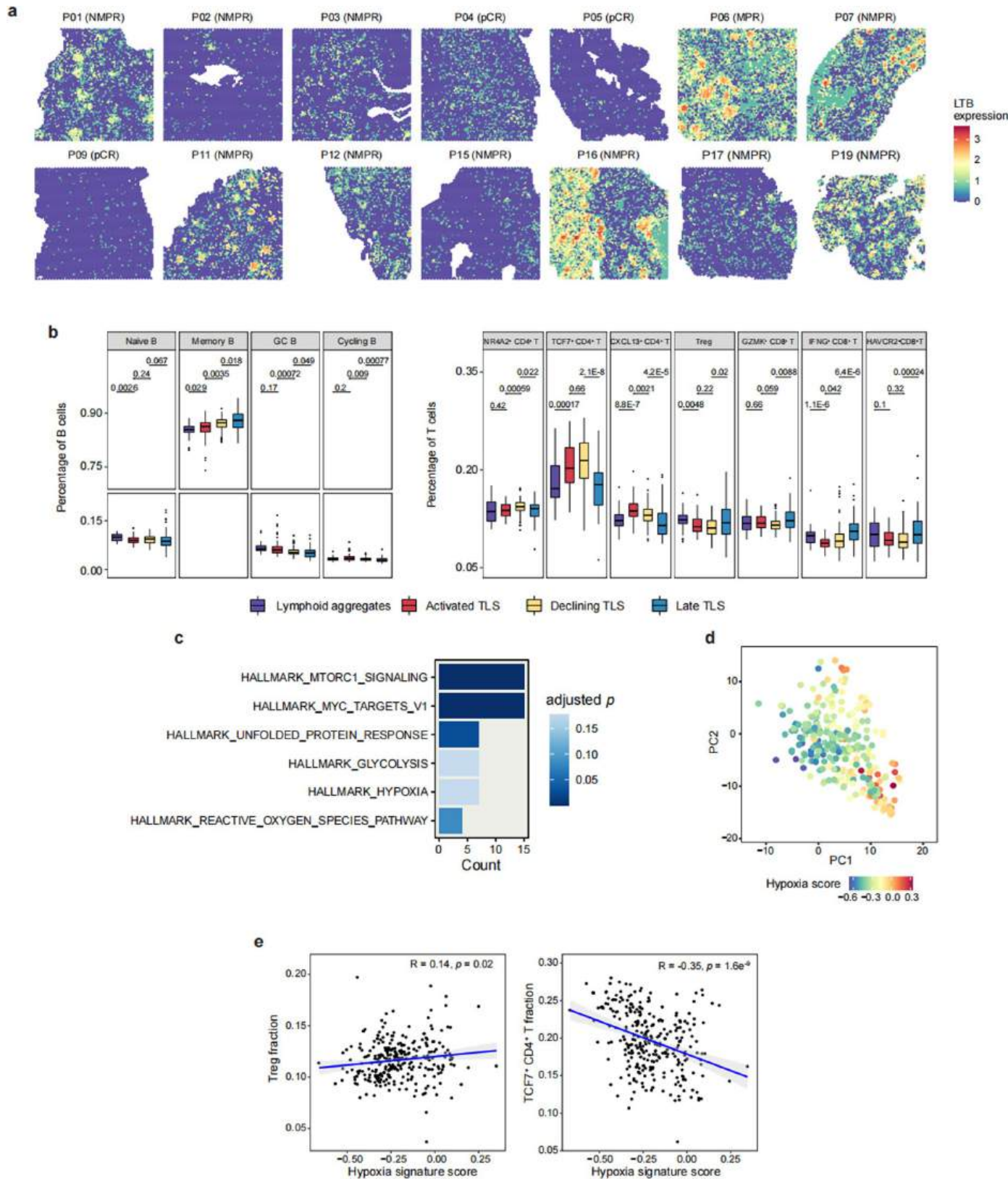
Extended Data Fig. 6 | Spatial distribution of T and B cells and identification of TLSs. **a**, The spatial distribution of T cells in patient 11 (P11). The darker red color represents a higher cell-type proportion. **b**, The spatial distribution of B cells P11. The darker red color represents a higher cell-type proportion. **c**, Boxplots showing the differences in T cell subtype proportions in tumor ($n = 150$), tumor boundary ($n = 162$) and stromal ($n = 3651$) regions in patient P11. Statistical significance was determined by two-sided Wilcoxon rank-sum test. ns: $P > 0.05$; *: $P < 0.05$; **: $P < 0.01$; ***: $P < 0.001$; ****: $P < 0.0001$. **d**, Heat-dot plot showing cell-type colocalizations in patient P11. Pearson correlations of the estimated cell-type proportions were calculated for each pair of cell types across all spots. The color and size of the dot represent the correlation coefficient. A positive correlation coefficient indicates colocalization of the cell-type pair, whereas negative values indicate exclusion of the two cell types from each other.

The black rectangle highlights the colocalization of T and B cells. **e**, Pathological examination of TLSs in patient P11. Scale bar: 1 mm. All Visium slides ($n = 17$) were examined. **f**, The automated TLS identification workflow named Space Scanner through combining H&E image and ST data. **g**, Location of identified TLSs in patient P11. Red and gray colors represent TLSs and surrounding stroma respectively. **h**, Heatmap showing the averaged expression of 12 chemokines in TLSs and stroma from patient P11. **i**, Boxplots showing the differences in B (left panels) and T (right panels) cell subtype proportions within TLSs ($n = 210$) and stroma ($n = 294$) in patient P11. Statistical significance was determined by two-sided Wilcoxon rank-sum test. ns: $P > 0.05$; *: $P < 0.05$; **: $P < 0.01$; ***: $P < 0.001$; ****: $P < 0.0001$. For the boxplots in **c** and **i**, the box limits denote the first and third quartiles, with the median shown in the center and whiskers covering data within $1.5 \times$ the interquartile range from the box.



Extended Data Fig. 7 | Spatial distributions of T and B cells and identification of TLSs. **a**, Spatial distributions of CD4 T cells, Treg and CD8 T cells, relative to tumor spots in patient P11. CD4 and CD8 T cell proportions were measured by the sum of the corresponding subtypes. The darker red color in the left 3 panels represents higher cell-type proportions. The right panel shows the definition of tumor spots, tumor-boundaries and stroma regions in patient

P11. **b**, The spatial distribution of T (top) and B cell proportions (middle) and the location of identified TLSs (bottom) in samples excluding P11. **c**, Cell-type compositions of the identified TLSs in 14 samples. The average proportions of all TLS spots were calculated to represent the cellular compositions of each TLS. Related to Extended Data Fig.6.



Extended Data Fig. 8 | See next page for caption.

Extended Data Fig. 8 | Characteristics of TLSs in different stages. **a**, Spatial distributions of LTB expression in all slides with TLSs. **b**, Boxplots showing the differences in B (left) and T (right) subtype proportions in TLSs at different stages from all samples. For each TLS, the average subtype proportions of covered spots were calculated to represent the cellular subtype proportions of each TLS. lymphoid aggregates, n = 42; Activated TLS, n = 71; Declining TLS, n = 103; Late TLS, n = 67. Statistical significance was determined by two-sided Wilcoxon rank-sum test. ns: P >= 0.05; *: P < 0.05; **: P < 0.01; ***: P < 0.001; ****: P < 0.0001. The box limits denote the first and third quartiles, with the median shown in the

center and whiskers covering data within $1.5 \times$ the interquartile range from the box. **c**, Bar plot showing the enriched Hallmark pathways in NMPR, related to Fig. 6h. The color represents the significance. A *P* value denotes the enrichment *P* value of the pathway ID determined by Fisher's exact test. **d**, PCA visualization of the hypoxia signature score in all TLSs. **e**, The correlation between the hypoxia signature score and the fraction of Treg (left) and CD4_TCF7 (right) in all TLSs. The blue lines are regression lines. The gray bands are 95% confidence bands for the regression line. Each dot represents an identified TLS. The two-sided *P* values was measured by Pearson's correlation test. Related to Fig. 6.

Reporting Summary

Nature Portfolio wishes to improve the reproducibility of the work that we publish. This form provides structure for consistency and transparency in reporting. For further information on Nature Portfolio policies, see our [Editorial Policies](#) and the [Editorial Policy Checklist](#).

Statistics

For all statistical analyses, confirm that the following items are present in the figure legend, table legend, main text, or Methods section.

n/a Confirmed

- The exact sample size (n) for each experimental group/condition, given as a discrete number and unit of measurement
- A statement on whether measurements were taken from distinct samples or whether the same sample was measured repeatedly
- The statistical test(s) used AND whether they are one- or two-sided
Only common tests should be described solely by name; describe more complex techniques in the Methods section.
- A description of all covariates tested
- A description of any assumptions or corrections, such as tests of normality and adjustment for multiple comparisons
- A full description of the statistical parameters including central tendency (e.g. means) or other basic estimates (e.g. regression coefficient) AND variation (e.g. standard deviation) or associated estimates of uncertainty (e.g. confidence intervals)
- For null hypothesis testing, the test statistic (e.g. F , t , r) with confidence intervals, effect sizes, degrees of freedom and P value noted
Give P values as exact values whenever suitable.
- For Bayesian analysis, information on the choice of priors and Markov chain Monte Carlo settings
- For hierarchical and complex designs, identification of the appropriate level for tests and full reporting of outcomes
- Estimates of effect sizes (e.g. Cohen's d , Pearson's r), indicating how they were calculated

Our web collection on [statistics for biologists](#) contains articles on many of the points above.

Software and code

Policy information about [availability of computer code](#)

Data collection	scRNA-seq FASTQ files were processed using the BD Rhapsody Whole Transcriptome Analysis (WTA) Pipeline and the CeleScope pipeline to get a unique molecular identifier (UMI) matrix for each sample. Raw bulk RNA-seq FASTQ files were aligned on the hg38 genome reference using the STAR aligner with default parameters. Salmon was used to quantitate gene expression by transcripts per kilobase million (TPM).
Data analysis	The scRNA-seq matrix of read counts per gene per sample was further analyzed by the Seurat package (version 3.2.2). To identify malignant cells from epithelia, we used the infercnvpy algorithm (version 0.2.0) to estimate the copy number variations (CNVs). Cell-cell interaction analysis was conducted using CellPhoneDB (version 2.1.5), SingleCellSignalR (version 1.0) and NicheNet (version 1.0.0). Gene module enrichment analysis was conducted using AUCell (version 1.8.0). The cell signatures were estimated by ssGSEA method in the GSVA R package (version 1.32.0). The analyses of lung adenocarcinoma (LUAD) from the TCGA database were performed on the TCGA visualization web server, GEPIA2 (http://gepia2.cancer-pku.cn/). The generated gene-by-spot matrices were analyzed with the Seurat package (version 4.0.4). Spatial transcriptomics downstream deconvolution analysis was conducted using STRIDE (version 0.0.1b). The TLS maturation trajectory analysis was conducted using Monocle2 (version 2.14.0). Random forest model analysis was conducted using R package 'randomForest' (version 4.7-1.1).

For manuscripts utilizing custom algorithms or software that are central to the research but not yet described in published literature, software must be made available to editors and reviewers. We strongly encourage code deposition in a community repository (e.g. GitHub). See the Nature Portfolio [guidelines for submitting code & software](#) for further information.

Data

Policy information about [availability of data](#)

All manuscripts must include a [data availability statement](#). This statement should provide the following information, where applicable:

- Accession codes, unique identifiers, or web links for publicly available datasets
- A description of any restrictions on data availability
- For clinical datasets or third party data, please ensure that the statement adheres to our [policy](#)

Raw single-cell RNA-seq and spatial Transcriptomics data are deposited to Genome Sequence Archive of the BIG Data Center at the Beijing Institute of Genomics, Chinese Academy of Science, under accession number HRA002509 (Accessible at <http://bigd.big.ac.cn/gsa-human/browse/HRA002509>).

Research involving human participants, their data, or biological material

Policy information about studies with [human participants or human data](#). See also policy information about [sex, gender \(identity/presentation\), and sexual orientation](#) and [race, ethnicity and racism](#).

Reporting on sex and gender	This study is mainly focused on the NSCLC microenvironment associated with resistance to immune-chemotherapy, so no gender-based analyses have been performed.
Reporting on race, ethnicity, or other socially relevant groupings	The socially relevant categorization variables have not been used in the manuscript, so no such analyses have been performed.
Population characteristics	19 patients who were diagnosed with NSCLC are included in this study. All of them received the anti-PD-1 antibody plus chemotherapy before undergoing surgical resection of NSCLC. Before recruitment, All participants were treatment-naïve and EGFR/ALK mutation negative. 3 of them are females, and 16 of them are males; 1 of patients were diagnosed at stage IB, 1 at IIB, 15 at IIIA, 1 at IIIB, 1 at IIIC. The age distribution is 45-75.
Recruitment	Treatment-naïve patients with stage IB-III NSCLC with EGFR/ALK mutation negative were identified in Department of Thoracic Surgery, Shanghai Pulmonary Hospital, and recruited for study. There was no potential self selection bias. Informed consent was obtained from all human research subjects.
Ethics oversight	All human studies performed in accordance with ethical regulation, and pre-approved by the Ethics Committee of Shanghai Pulmonary Hospital (No. K21-294).

Note that full information on the approval of the study protocol must also be provided in the manuscript.

Field-specific reporting

Please select the one below that is the best fit for your research. If you are not sure, read the appropriate sections before making your selection.

Life sciences Behavioural & social sciences Ecological, evolutionary & environmental sciences

For a reference copy of the document with all sections, see nature.com/documents/nr-reporting-summary-flat.pdf

Life sciences study design

All studies must disclose on these points even when the disclosure is negative.

Sample size	No statistical method was used to determine the patient sample size. The number of patient samples was primarily determined by the availability of tumor samples in the trials and achievement of sequencing.
Data exclusions	For scRNAseq, low quality cells with low number of expressed genes or high proportion of mitochondrial gene counts or doublets were excluded from the dataset. For Spatial transcriptomic analysis, slides with bad-quality matched H&E image are excluded from the dataset.
Replication	The single-cell RNA-Sequencing and spatial transcriptomics experiments described in this study consisted of an independent single replicate per patient tumor. This was primarily due to the limited tissue samples collected from clinical specimens as well as funding limitations and is typical for this field. However, the transcriptional signatures of the single-cell clusters identified in our dataset were consistent with prior studies.
Randomization	The patients in this study received Anti-PD-1 therapy and its design is not based on randomization. All the patients were treated with PD-1 antibody combined with chemotherapy. Previous studies have shown that it is the PD-1 pathway blockade that affect the state transition of tumour-reactive T cells (Beltra et al, 2020), and this effect is therefore unlikely associated with covariates like age and gender. In addition, the comparisons between pre- and post-treatment samples were well controlled because these samples were from the same patients and were site-matched. Therefore, the covariates were not controlled.
Blinding	Blinding was not relevant in our study as samples were collected from patients as they came into the clinic. As every sample was included in the study and processed in the same standardized way, knowledge of clinical phenotypes would not affect the study.

Behavioural & social sciences study design

All studies must disclose on these points even when the disclosure is negative.

Study description	<i>Briefly describe the study type including whether data are quantitative, qualitative, or mixed-methods (e.g. qualitative cross-sectional, quantitative experimental, mixed-methods case study).</i>
Research sample	<i>State the research sample (e.g. Harvard university undergraduates, villagers in rural India) and provide relevant demographic information (e.g. age, sex) and indicate whether the sample is representative. Provide a rationale for the study sample chosen. For studies involving existing datasets, please describe the dataset and source.</i>
Sampling strategy	<i>Describe the sampling procedure (e.g. random, snowball, stratified, convenience). Describe the statistical methods that were used to predetermine sample size OR if no sample-size calculation was performed, describe how sample sizes were chosen and provide a rationale for why these sample sizes are sufficient. For qualitative data, please indicate whether data saturation was considered, and what criteria were used to decide that no further sampling was needed.</i>
Data collection	<i>Provide details about the data collection procedure, including the instruments or devices used to record the data (e.g. pen and paper, computer, eye tracker, video or audio equipment) whether anyone was present besides the participant(s) and the researcher, and whether the researcher was blind to experimental condition and/or the study hypothesis during data collection.</i>
Timing	<i>Indicate the start and stop dates of data collection. If there is a gap between collection periods, state the dates for each sample cohort.</i>
Data exclusions	<i>If no data were excluded from the analyses, state so OR if data were excluded, provide the exact number of exclusions and the rationale behind them, indicating whether exclusion criteria were pre-established.</i>
Non-participation	<i>State how many participants dropped out/declined participation and the reason(s) given OR provide response rate OR state that no participants dropped out/declined participation.</i>
Randomization	<i>If participants were not allocated into experimental groups, state so OR describe how participants were allocated to groups, and if allocation was not random, describe how covariates were controlled.</i>

Ecological, evolutionary & environmental sciences study design

All studies must disclose on these points even when the disclosure is negative.

Study description	<i>Briefly describe the study. For quantitative data include treatment factors and interactions, design structure (e.g. factorial, nested, hierarchical), nature and number of experimental units and replicates.</i>
Research sample	<i>Describe the research sample (e.g. a group of tagged Passer domesticus, all Stenocereus thurberi within Organ Pipe Cactus National Monument), and provide a rationale for the sample choice. When relevant, describe the organism taxa, source, sex, age range and any manipulations. State what population the sample is meant to represent when applicable. For studies involving existing datasets, describe the data and its source.</i>
Sampling strategy	<i>Note the sampling procedure. Describe the statistical methods that were used to predetermine sample size OR if no sample-size calculation was performed, describe how sample sizes were chosen and provide a rationale for why these sample sizes are sufficient.</i>
Data collection	<i>Describe the data collection procedure, including who recorded the data and how.</i>
Timing and spatial scale	<i>Indicate the start and stop dates of data collection, noting the frequency and periodicity of sampling and providing a rationale for these choices. If there is a gap between collection periods, state the dates for each sample cohort. Specify the spatial scale from which the data are taken.</i>
Data exclusions	<i>If no data were excluded from the analyses, state so OR if data were excluded, describe the exclusions and the rationale behind them, indicating whether exclusion criteria were pre-established.</i>
Reproducibility	<i>Describe the measures taken to verify the reproducibility of experimental findings. For each experiment, note whether any attempts to repeat the experiment failed OR state that all attempts to repeat the experiment were successful.</i>
Randomization	<i>Describe how samples/organisms/participants were allocated into groups. If allocation was not random, describe how covariates were controlled. If this is not relevant to your study, explain why.</i>
Blinding	<i>Describe the extent of blinding used during data acquisition and analysis. If blinding was not possible, describe why OR explain why blinding was not relevant to your study.</i>

Did the study involve field work? Yes No

Field work, collection and transport

Field conditions	Describe the study conditions for field work, providing relevant parameters (e.g. temperature, rainfall).
Location	State the location of the sampling or experiment, providing relevant parameters (e.g. latitude and longitude, elevation, water depth).
Access & import/export	Describe the efforts you have made to access habitats and to collect and import/export your samples in a responsible manner and in compliance with local, national and international laws, noting any permits that were obtained (give the name of the issuing authority, the date of issue, and any identifying information).
Disturbance	Describe any disturbance caused by the study and how it was minimized.

Reporting for specific materials, systems and methods

We require information from authors about some types of materials, experimental systems and methods used in many studies. Here, indicate whether each material, system or method listed is relevant to your study. If you are not sure if a list item applies to your research, read the appropriate section before selecting a response.

Materials & experimental systems		Methods	
n/a	Involved in the study	n/a	Involved in the study
<input type="checkbox"/>	<input checked="" type="checkbox"/> Antibodies	<input checked="" type="checkbox"/>	<input type="checkbox"/> ChIP-seq
<input checked="" type="checkbox"/>	<input type="checkbox"/> Eukaryotic cell lines	<input checked="" type="checkbox"/>	<input type="checkbox"/> Flow cytometry
<input checked="" type="checkbox"/>	<input type="checkbox"/> Palaeontology and archaeology	<input checked="" type="checkbox"/>	<input type="checkbox"/> MRI-based neuroimaging
<input checked="" type="checkbox"/>	<input type="checkbox"/> Animals and other organisms		
<input checked="" type="checkbox"/>	<input type="checkbox"/> Clinical data		
<input checked="" type="checkbox"/>	<input type="checkbox"/> Dual use research of concern		
<input checked="" type="checkbox"/>	<input type="checkbox"/> Plants		

Antibodies

Antibodies used	Anti-human COL11A1 Proteintech, 21841-1-AP Anti-human DDR1 CST, 5583 Anti-human α-SMA Abcam, ab5694 Anti-human Pan-CK SIGMA-ALDRICH, C2562 Anti-human FAP Abcam, ab222924 Anti-human CD3 Abcam, ab135372 Anti-human SPP1 CST, 88742
Validation	All the antibodies used in this study were commercial available antibodies, with validation procedures described on the manufacturer's websites as below: Anti-human COL11A1 Proteintech, 21841-1-AP (https://www.thermofisher.cn/cn/zh/antibody/product/Collagen-Type-XI-Antibody-Polyclonal/21841-1-AP ; validated in human for IHC) Anti-human DDR1 CST, 5583 (https://www.cellsignal.com/products/primary-antibodies/ddr1-d1g6-xp-rabbit-mab/5583 ; validated in human for IHC) Anti-human α-SMA Abcam, ab5694 (https://www.abcam.com/products/primary-antibodies/alpha-smooth-muscle-actin-antibody-ab5694.html) Anti-human FAP Abcam, ab222924 (https://www.abcam.cn/products/primary-antibodies/fibroblast-activation-protein-alpha-antibody-epr20021-low-endotoxin-azide-free-ab222924.html) Anti-human Pan-CK SIGMA-ALDRICH, C2562 (https://www.sigmaldrich.cn/CN/zh/product/sigma/c2562) Anti-human CD3 Abcam, ab135372 (https://www.abcam.cn/products/primary-antibodies/cd3-antibody-sp162-ab135372.html) Anti-human SPP1 CST, 88742 (https://www.cellsignal.cn/products/primary-antibodies/osteopontin-spp1-e9z1d-rabbit-mab/88742)

Eukaryotic cell lines

Policy information about [cell lines and Sex and Gender in Research](#)

Cell line source(s)	State the source of each cell line used and the sex of all primary cell lines and cells derived from human participants or vertebrate models.
Authentication	Describe the authentication procedures for each cell line used OR declare that none of the cell lines used were authenticated.
Mycoplasma contamination	Confirm that all cell lines tested negative for mycoplasma contamination OR describe the results of the testing for mycoplasma contamination OR declare that the cell lines were not tested for mycoplasma contamination.

Palaeontology and Archaeology

Specimen provenance	Provide provenance information for specimens and describe permits that were obtained for the work (including the name of the issuing authority, the date of issue, and any identifying information). Permits should encompass collection and, where applicable, export.
Specimen deposition	Indicate where the specimens have been deposited to permit free access by other researchers.
Dating methods	If new dates are provided, describe how they were obtained (e.g. collection, storage, sample pretreatment and measurement), where they were obtained (i.e. lab name), the calibration program and the protocol for quality assurance OR state that no new dates are provided.

Tick this box to confirm that the raw and calibrated dates are available in the paper or in Supplementary Information.

Ethics oversight	Identify the organization(s) that approved or provided guidance on the study protocol, OR state that no ethical approval or guidance was required and explain why not.
------------------	--

Note that full information on the approval of the study protocol must also be provided in the manuscript.

Animals and other research organisms

Policy information about [studies involving animals; ARRIVE guidelines](#) recommended for reporting animal research, and [Sex and Gender in Research](#)

Laboratory animals	For laboratory animals, report species, strain and age OR state that the study did not involve laboratory animals.
Wild animals	Provide details on animals observed in or captured in the field; report species and age where possible. Describe how animals were caught and transported and what happened to captive animals after the study (if killed, explain why and describe method; if released, say where and when) OR state that the study did not involve wild animals.
Reporting on sex	Indicate if findings apply to only one sex; describe whether sex was considered in study design, methods used for assigning sex. Provide data disaggregated for sex where this information has been collected in the source data as appropriate; provide overall numbers in this Reporting Summary. Please state if this information has not been collected. Report sex-based analyses where performed, justify reasons for lack of sex-based analysis.
Field-collected samples	For laboratory work with field-collected samples, describe all relevant parameters such as housing, maintenance, temperature, photoperiod and end-of-experiment protocol OR state that the study did not involve samples collected from the field.
Ethics oversight	Identify the organization(s) that approved or provided guidance on the study protocol, OR state that no ethical approval or guidance was required and explain why not.

Note that full information on the approval of the study protocol must also be provided in the manuscript.

Clinical data

Policy information about [clinical studies](#)

All manuscripts should comply with the ICMJE [guidelines for publication of clinical research](#) and a completed [CONSORT checklist](#) must be included with all submissions.

Clinical trial registration	Provide the trial registration number from ClinicalTrials.gov or an equivalent agency.
Study protocol	Note where the full trial protocol can be accessed OR if not available, explain why.
Data collection	Describe the settings and locales of data collection, noting the time periods of recruitment and data collection.
Outcomes	Describe how you pre-defined primary and secondary outcome measures and how you assessed these measures.

Dual use research of concern

Policy information about [dual use research of concern](#)

Hazards

Could the accidental, deliberate or reckless misuse of agents or technologies generated in the work, or the application of information presented in the manuscript, pose a threat to:

No	Yes
<input type="checkbox"/>	<input type="checkbox"/> Public health
<input type="checkbox"/>	<input type="checkbox"/> National security
<input type="checkbox"/>	<input type="checkbox"/> Crops and/or livestock
<input type="checkbox"/>	<input type="checkbox"/> Ecosystems
<input type="checkbox"/>	<input type="checkbox"/> Any other significant area

Experiments of concern

Does the work involve any of these experiments of concern:

No	Yes
<input type="checkbox"/>	<input type="checkbox"/> Demonstrate how to render a vaccine ineffective
<input type="checkbox"/>	<input type="checkbox"/> Confer resistance to therapeutically useful antibiotics or antiviral agents
<input type="checkbox"/>	<input type="checkbox"/> Enhance the virulence of a pathogen or render a nonpathogen virulent
<input type="checkbox"/>	<input type="checkbox"/> Increase transmissibility of a pathogen
<input type="checkbox"/>	<input type="checkbox"/> Alter the host range of a pathogen
<input type="checkbox"/>	<input type="checkbox"/> Enable evasion of diagnostic/detection modalities
<input type="checkbox"/>	<input type="checkbox"/> Enable the weaponization of a biological agent or toxin
<input type="checkbox"/>	<input type="checkbox"/> Any other potentially harmful combination of experiments and agents

Plants

Seed stocks

Not available

Novel plant genotypes

Not available

Authentication

Not available

ChIP-seq

Data deposition

- Confirm that both raw and final processed data have been deposited in a public database such as [GEO](#).
- Confirm that you have deposited or provided access to graph files (e.g. BED files) for the called peaks.

Data access links

May remain private before publication.

For "Initial submission" or "Revised version" documents, provide reviewer access links. For your "Final submission" document, provide a link to the deposited data.

Files in database submission

Provide a list of all files available in the database submission.

Genome browser session
(e.g. [UCSC](#))

Provide a link to an anonymized genome browser session for "Initial submission" and "Revised version" documents only, to enable peer review. Write "no longer applicable" for "Final submission" documents.

Methodology

Replicates

Describe the experimental replicates, specifying number, type and replicate agreement.

Sequencing depth

Describe the sequencing depth for each experiment, providing the total number of reads, uniquely mapped reads, length of reads and whether they were paired- or single-end.

Antibodies

Describe the antibodies used for the ChIP-seq experiments; as applicable, provide supplier name, catalog number, clone name, and lot number.

Peak calling parameters

Specify the command line program and parameters used for read mapping and peak calling, including the ChIP, control and index files used.

Data quality

Describe the methods used to ensure data quality in full detail, including how many peaks are at FDR 5% and above 5-fold enrichment.

Software

Describe the software used to collect and analyze the ChIP-seq data. For custom code that has been deposited into a community repository, provide accession details.

Flow Cytometry

Plots

Confirm that:

- The axis labels state the marker and fluorochrome used (e.g. CD4-FITC).
- The axis scales are clearly visible. Include numbers along axes only for bottom left plot of group (a 'group' is an analysis of identical markers).
- All plots are contour plots with outliers or pseudocolor plots.
- A numerical value for number of cells or percentage (with statistics) is provided.

Methodology

Sample preparation

Describe the sample preparation, detailing the biological source of the cells and any tissue processing steps used.

Instrument

Identify the instrument used for data collection, specifying make and model number.

Software

Describe the software used to collect and analyze the flow cytometry data. For custom code that has been deposited into a community repository, provide accession details.

Cell population abundance

Describe the abundance of the relevant cell populations within post-sort fractions, providing details on the purity of the samples and how it was determined.

Gating strategy

Describe the gating strategy used for all relevant experiments, specifying the preliminary FSC/SSC gates of the starting cell population, indicating where boundaries between "positive" and "negative" staining cell populations are defined.

Tick this box to confirm that a figure exemplifying the gating strategy is provided in the Supplementary Information.

Magnetic resonance imaging

Experimental design

Design type

Indicate task or resting state; event-related or block design.

Design specifications

Specify the number of blocks, trials or experimental units per session and/or subject, and specify the length of each trial or block (if trials are blocked) and interval between trials.

Behavioral performance measures

State number and/or type of variables recorded (e.g. correct button press, response time) and what statistics were used to establish that the subjects were performing the task as expected (e.g. mean, range, and/or standard deviation across subjects).

Acquisition

Imaging type(s)

Specify: functional, structural, diffusion, perfusion.

Field strength

Specify in Tesla

Sequence & imaging parameters

Specify the pulse sequence type (gradient echo, spin echo, etc.), imaging type (EPI, spiral, etc.), field of view, matrix size, slice thickness, orientation and TE/TR/flip angle.

Area of acquisition

State whether a whole brain scan was used OR define the area of acquisition, describing how the region was determined.

Diffusion MRI

Used

Not used

Preprocessing

Preprocessing software

Provide detail on software version and revision number and on specific parameters (model/functions, brain extraction, segmentation, smoothing kernel size, etc.).

Normalization

If data were normalized/standardized, describe the approach(es): specify linear or non-linear and define image types used for transformation OR indicate that data were not normalized and explain rationale for lack of normalization.

Normalization template

Describe the template used for normalization/transformation, specifying subject space or group standardized space (e.g. original Talairach, MNI305, ICBM152) OR indicate that the data were not normalized.

Noise and artifact removal

Describe your procedure(s) for artifact and structured noise removal, specifying motion parameters, tissue signals and physiological signals (heart rate, respiration).

Volume censoring

Define your software and/or method and criteria for volume censoring, and state the extent of such censoring.

Statistical modeling & inference**Model type and settings**

Specify type (mass univariate, multivariate, RSA, predictive, etc.) and describe essential details of the model at the first and second levels (e.g. fixed, random or mixed effects; drift or auto-correlation).

Effect(s) tested

Define precise effect in terms of the task or stimulus conditions instead of psychological concepts and indicate whether ANOVA or factorial designs were used.

Specify type of analysis: Whole brain ROI-based Both

Statistic type for inference

Specify voxel-wise or cluster-wise and report all relevant parameters for cluster-wise methods.

(See [Eklund et al. 2016](#))

Correction

Describe the type of correction and how it is obtained for multiple comparisons (e.g. FWE, FDR, permutation or Monte Carlo).

Models & analysis**n/a**

- Involved in the study
- Functional and/or effective connectivity
- Graph analysis
- Multivariate modeling or predictive analysis

Functional and/or effective connectivity

Report the measures of dependence used and the model details (e.g. Pearson correlation, partial correlation, mutual information).

Graph analysis

Report the dependent variable and connectivity measure, specifying weighted graph or binarized graph, subject- or group-level, and the global and/or node summaries used (e.g. clustering coefficient, efficiency, etc.).

Multivariate modeling and predictive analysis

Specify independent variables, features extraction and dimension reduction, model, training and evaluation metrics.